



## Article

# Highly Efficient Visible-Light Photocatalysts: $\text{Bi}_2\text{O}_3@\text{TiO}_2$ Derived from Ti-MOFs for Eriochrome Black T Degradation: A Joint Experimental and Computational Study

Jing Meng<sup>1,†</sup>, Asmaa G. Ashry<sup>2,†</sup>, Ahmed S. Abou-Elyazed<sup>2,3,\*</sup> , Zhe Zhang<sup>1</sup>, Xiaolin Li<sup>3,\*</sup>, Tamer Z. Sharara<sup>4</sup> and Safinaz H. El-Demerdash<sup>2</sup> 

<sup>1</sup> School of Civil Engineering, Nantong Institute of Technology, Nantong 226002, China; mengjing@ntit.edu.cn (J.M.); 20239078@ntit.edu.cn (Z.Z.)

<sup>2</sup> Chemistry Department, Faculty of Science, Menoufia University, Shebin El-Kom 32511, Egypt; asmaaashry137@yahoo.com (A.G.A.); hamdysafinaz@yahoo.com (S.H.E.-D.)

<sup>3</sup> Institute of Intelligent Manufacturing Technology, Shenzhen Polytechnic University, Shenzhen 518055, China

<sup>4</sup> EPRI Nanotechnology Center, Egyptian Petroleum Research Institute, Nasr City, Cairo 11727, Egypt; tamerzakisharara@yahoo.com

\* Correspondence: ahmedphysical90@gmail.com (A.S.A.-E.); lixiaolin0427@szpu.edu.cn (X.L.)

† These authors contributed equally to this work.

**Abstract:** Herein, we synthesized Ti-MOF through a solvothermal method and subsequently calcined it to form anatase  $\text{TiO}_2$ . We further developed a  $\text{Bi}_2\text{O}_3@\text{TiO}_2$  mixed oxide using impregnation and calcination processes. These oxides showed significant photocatalytic activity for degrading Eriochrome Black T (EBT) dye under visible light irradiation. We characterized the prepared samples using various techniques, including XRD, XPS, FTIR, BET, SEM, EDX, TEM, and UV-DRS analyses. Our results indicated that  $\text{TiO}_2$  and 10% $\text{Bi}_2\text{O}_3@\text{TiO}_2$  achieved 80% and 100% degradation of EBT dye solution (50 ppm) within 30 min in acidic medium with a 50 mg catalyst dose, respectively. The calcination of the Ti-MOF into  $\text{TiO}_2$  improved its sensitivity to visible light. The  $\text{Bi}_2\text{O}_3@\text{TiO}_2$  composite was also effective in degrading other organic pollutants, such as Congo Red (degradation ~99%), Malachite Green (degradation ~95%), Methylene Blue (degradation ~81%), and Safranin O (degradation ~69%). The impregnation of  $\text{Bi}_2\text{O}_3$  increased the surface acidity of  $\text{TiO}_2$ , enhancing its photocatalytic activity by promoting hydroxyl group formation through increased water adsorption. Additionally, 10% $\text{Bi}_2\text{O}_3@\text{TiO}_2$  demonstrated excellent chemical stability and reusability, maintaining high degradation efficiency over four cycles. Density Functional Theory (DFT) and Time-Dependent DFT (TD-DFT) calculations were performed to understand the degradation mechanisms. UV-Vis absorption spectrum simulations suggested that the anionic  $\text{HEB}^{-2}$  ( $\text{O}_2\text{A}$ ) or  $\text{EB}^{-3}$  forms of the EBT dye are likely to undergo degradation. This study highlights the potential of  $\text{Bi}_2\text{O}_3@\text{TiO}_2$  composites for effective photocatalytic applications in environmental remediation.

**Keywords:** Ti-MOF; calcination; mixed oxides; photocatalytic degradation; EBT



**Citation:** Meng, J.; Ashry, A.G.; Abou-Elyazed, A.S.; Zhang, Z.; Li, X.; Sharara, T.Z.; El-Demerdash, S.H. Highly Efficient Visible-Light Photocatalysts:  $\text{Bi}_2\text{O}_3@\text{TiO}_2$  Derived from Ti-MOFs for Eriochrome Black T Degradation: A Joint Experimental and Computational Study. *Catalysts* **2024**, *14*, 829. <https://doi.org/10.3390/catal14110829>

Academic Editor: Christos Trapalis

Received: 8 October 2024

Revised: 14 November 2024

Accepted: 15 November 2024

Published: 17 November 2024



**Copyright:** © 2024 by the authors. Licensee MDPI, Basel, Switzerland. This article is an open access article distributed under the terms and conditions of the Creative Commons Attribution (CC BY) license (<https://creativecommons.org/licenses/by/4.0/>).

## 1. Introduction

One of the most pressing challenges in recent years has been the significant increase in environmental pollution, with water pollution being a primary concern [1]. Industrial activities and chemical-based industries have introduced vast amounts of harmful chemicals into the environment, damaging various ecosystems. Among these pollutants, dyes, heavy metals, chloro-organics, and pharmaceuticals are major sources of aquatic contamination [2]. Conventional water treatment methods such as biological treatment, sedimentation, filtration, and membrane technologies often merely transfer contaminants from one medium to another, involve high operational costs, require substantial time, and may release secondary pollutants into the ecosystem [3,4].

Over the past several years, photocatalysis has emerged as an effective, affordable, and environmentally friendly technology for removing hazardous pollutants. Photocatalysis offers advantages such as catalyst regeneration and reuse, operation under ambient conditions, and the capability to degrade a wide spectrum of organic contaminants [5,6]. However, conventional photocatalysts are limited by their absorption of light primarily in the UV spectrum (which constitutes only 4% of the solar spectrum) and rapid charge recombination. To more effectively harness the solar spectrum, advanced photocatalyst systems that can be activated by visible light need to be developed [7].

Eriochrome Black T (EBT) is an anionic azo dye widely used in complexometric titrations and the dyeing of wool, leather, and nylon in textile manufacturing [8,9]. EBT is soluble in water and can cause skin, bladder, and gastrointestinal disorders, as well as iron deficiency [10]. Due to its extensive industrial use, EBT is considered a significant environmental pollutant in water. Considerable efforts have been made to mitigate its impact and remove it from water. For instance, Sushil et al. demonstrated the photocatalytic degradation of EBT using TiO<sub>2</sub> nanoparticles under UV irradiation, achieving 82% degradation in 90 min [11]. Similarly, Malika et al. used chitosan for EBT removal, and the percentage of EBT removal rose to 96.77% in acidic medium by using 3 g/L of chitosan [12]. Additionally, Singh et al. prepared ZnO/Arg-Au/Cit nanocomposite for the removal of 65% of EBT in 2 h [13]. Previous research revealed significant limitations such as the use of limited UV irradiation, a long breakdown time, and a poor pH range; in addition, their performance was limited by the small surface area and pore volume. However, in this study, the TiO<sub>2</sub> and mixed oxides produced with a wide surface area and pore volume demonstrated excellent efficiency towards the total photocatalytic degradation of EBT in a very short time under visible light irradiation.

In recent years, metal-organic frameworks (MOFs) and their modifications have shown promise in photocatalytic dye degradation due to their unique properties, including tunable structures, low crystal densities, and large specific surface areas [14]. Among these, Ti-MOFs such as MIL-125, synthesized from terephthalic acid ligands and Ti-oxo clusters, have garnered significant attention [15]. Various modification strategies, including photosensitization, functional group modification, metal ion doping, and combination with optically active inorganic materials, have been employed to enhance their optical properties [16–18]. For example, BiOBr/NH<sub>2</sub>-MIL-125(Ti) composites degraded 80% of Rhodamine B under visible light illumination over 100 min [19], and Ag/AgBr/NH<sub>2</sub>-MIL-125(Ti) composites have shown strong photocatalytic activity towards methyl orange as the percent degradation reached 70% in 120 min under visible light irradiation [20]. Bi<sub>2</sub>WO<sub>6</sub>/MIL-125(Ti) composite enhanced the photocatalytic degradation of tetracycline hydrochloride (TC) to 73% under visible irradiation for 80 min [21]. Furthermore, Jian et al. prepared g-C<sub>3</sub>N<sub>4</sub>/TiO<sub>2</sub> with a Z-type heterojunction for the photocatalytic degradation of Methylene Blue (MB), and the decolorization ratio was 97.7% after 150 min of visible light irradiation [22].

In this work, we prepared MIL-125(Ti) via a solvothermal method and used it as a precursor to form titanium dioxide and mixed bismuth metal oxides through post-synthetic modification by impregnation followed by calcination. Various techniques, including X-ray diffraction (XRD), Fourier transform infrared (FTIR) spectroscopy, X-ray photoelectron spectroscopy (XPS), Brunauer–Emmett–Teller (BET) surface area analysis, scanning electron microscopy (SEM-EDX), transmission electron microscopy (TEM), and UV-Vis diffuse reflectance spectroscopy (DRS), were used to characterize the prepared materials. The photocatalytic degradation of Eriochrome Black T (EBT) dye was evaluated to determine their photocatalytic activity, and the effects of parameters such as the irradiation time, catalyst dosage, initial dye concentration, and pH were systematically studied. A photocatalytic mechanism is proposed, and the photocatalytic activity of the materials towards other organic pollutants, including Congo Red, Malachite Green, Methylene Blue, and Safranin O, is also discussed.

## 2. Results and Discussion

### 2.1. Structural Characterizations

The X-ray diffraction (XRD) patterns of the prepared samples are presented in Figure 1a. The XRD pattern of MIL-125(Ti) exhibits well-defined diffraction peaks at  $2\theta$  angles of  $7^\circ$ ,  $10^\circ$ ,  $12^\circ$ ,  $15.3^\circ$ ,  $16.9^\circ$ ,  $22.6^\circ$ ,  $26.24^\circ$ ,  $33.6^\circ$ ,  $48.7^\circ$ ,  $63.3^\circ$ ,  $78.4^\circ$ , and  $83.6^\circ$ , confirming its crystalline structure [23,24]. The XRD pattern of  $\text{TiO}_2$ , on the other hand, displays characteristic peaks at  $2\theta$  angles of  $25.5^\circ$ ,  $37.9^\circ$ ,  $48.2^\circ$ ,  $54.2^\circ$ ,  $55.1^\circ$ ,  $62.8^\circ$ ,  $69.02^\circ$ ,  $70.2^\circ$ , and  $75.5^\circ$ , indicating that the MIL-125 framework was transformed into anatase  $\text{TiO}_2$  after calcination. In the XRD patterns of  $\text{Bi}_2\text{O}_3@/\text{TiO}_2$  mixed oxides, additional peaks appear at  $27.7^\circ$ ,  $35.0^\circ$ ,  $45.5^\circ$ , and  $78.3^\circ$ . Notably, the peak at  $27.7^\circ$  broadens as the  $\text{Bi}_2\text{O}_3$  content increases from 10% to 30%, suggesting that different amounts of Bi species are incorporated into the mixed oxide samples. The catalytic performance data (Figure 1b) for materials with varying Bi ratios reveal that a 10%  $\text{Bi}_2\text{O}_3$  content provides the best balance between performance and economic feasibility, with no significant performance difference observed at higher Bi ratios. Consequently, 10%  $\text{Bi}_2\text{O}_3@/\text{TiO}_2$  is selected as the representative sample for further studies.

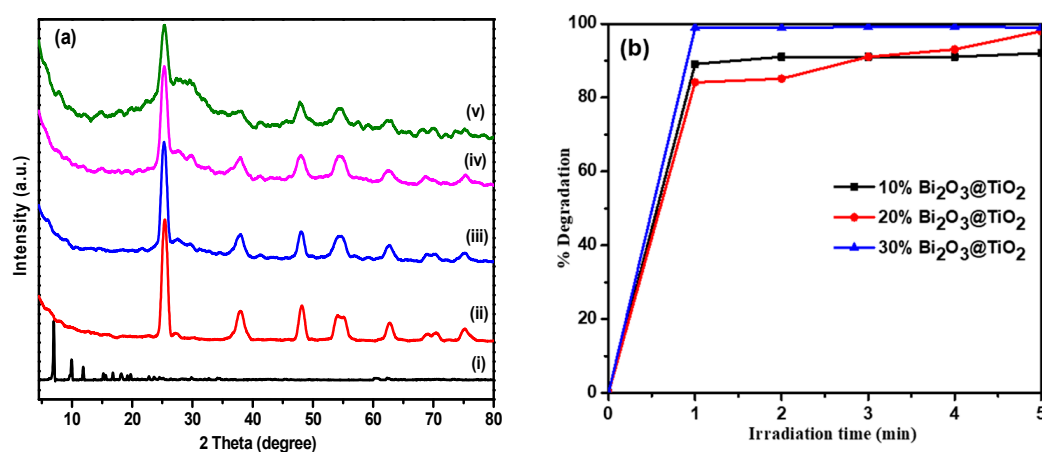


**Figure 1.** (a) XRD patterns of (i) MIL-125, (ii)  $\text{TiO}_2$ , and (iii, iv, v) 10, 20, and 30%  $\text{Bi}_2\text{O}_3@/\text{TiO}_2$ , respectively. (b) Effect of different ratio of  $\text{Bi}_2\text{O}_3$  on the degradation of EBT dye.

Further, the chemical composition and surface atom environments of the photocatalysts were characterized by the XPS technique (Figure 2). Figure 2a illustrates how the binding energies for Ti 2p, C 1s, and O 1s were visible in the scanning spectra for all samples; additionally, the binding energy of Bi 4f (159.1 eV and 164.5 eV) only appears in the 10%  $\text{Bi}_2\text{O}_3@/\text{TiO}_2$  sample, which closely matches the findings of the elemental mapping (EDX). For MIL-125, the peaks at 458.6 eV and 464.37 eV correspond to the binding energies of Ti  $2p_{3/2}$  and Ti  $2p_{1/2}$ , respectively, proving the existence of Ti-O bonds (Figure 2b). In contrast, these peaks for  $\text{TiO}_2$  and 10%  $\text{Bi}_2\text{O}_3@/\text{TiO}_2$  are slightly shifted with a difference of ca. 0.2 eV and ca. 0.1 eV, respectively, for Ti  $2p_{3/2}$  and ca. 0.07 eV and ca. 0.08 eV differences for Ti  $2p_{1/2}$ , respectively. Figure 2c,d shows similar results for the binding energies of O 1s and C 1s. The results support the XRD findings and indicate that the  $\text{Bi}^{3+}$  oxidation state of  $\text{Bi}_2\text{O}_3$  ought to be present in the structure of  $\text{TiO}_2$  based on the mixed oxide photocatalyst. This is also further explained by the binding energies at 159.1 eV and 164.5 eV fitted with Bi  $4f_{7/2}$  and Bi  $4f_{5/2}$ , respectively, for 10%  $\text{Bi}_2\text{O}_3@/\text{TiO}_2$  (Figure 2e) [25]. Figure 2f shows that Bi was impregnated by atomic weight percent 4.48%. The visible drop in carbon content and increase in oxygen content of the calcined samples further confirm the formation of metal oxides.

The FTIR spectra of MIL-125,  $\text{TiO}_2$ , and 10%  $\text{Bi}_2\text{O}_3@/\text{TiO}_2$  were supplied to elucidate the functional groups in the prepared photocatalysts as exhibited in Figure 3. The wide and strong absorption band at approximately  $3434\text{ cm}^{-1}$  was attributed to the asymmetrical and symmetrical stretching vibrations of the O-H group of the adsorbed water molecules

on the surface of the samples. For the MIL-125 spectra, the presence of a dicarboxylate linker in the produced Ti-MOF is associated with the peaks at  $1711\text{ cm}^{-1}$  and  $1272\text{ cm}^{-1}$ . The peaks around  $873\text{ cm}^{-1}$  are associated with Ti-O stretching for the non-bound (free coordinated) oxygen atom of the carboxylic groups of the BDC linker. The peaks at  $740$ ,  $677$ , and  $537\text{ cm}^{-1}$  are assigned to Ti-O-Ti stretching vibrations [26]. For the metal oxides spectra, peaks in the  $500\text{--}800\text{ cm}^{-1}$  range are attributed to the vibration absorption of the Ti-O-Ti bond in  $\text{TiO}_2$  and represent the contribution of anatase titania [27]; this matches with the results of the XRD analysis. At  $1601\text{ cm}^{-1}$ , a deformative vibration of the Ti-OH stretching mode can be noticed. The impregnation of Bi affected the intensity of the peaks and increased their sharpness in the  $10\%$   $\text{Bi}_2\text{O}_3@\text{TiO}_2$  sample, and the vibration of Bi-O appears at  $617.5\text{ cm}^{-1}$ .

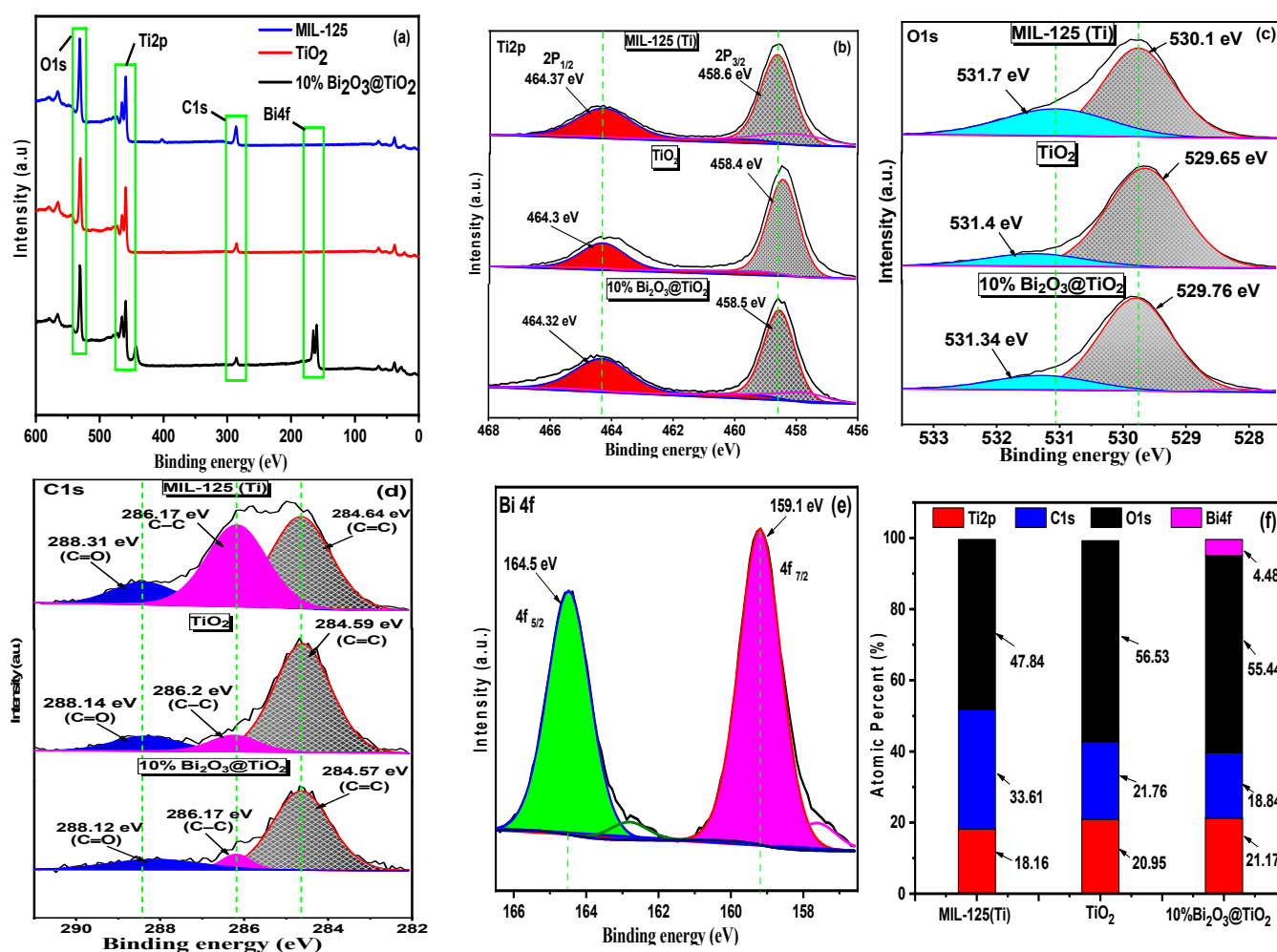


**Figure 2.** XPS analysis of various samples: (a) survey spectra of elements; (b) Ti 2p spectra; (c) O 1s spectra; (d) C 1s spectra; (e) Bi 4f spectra; (f) element contents.

The  $\text{NH}_3$ -TPD analysis was conducted to evaluate the strength and quantity of surface acid sites on  $10\%$   $\text{Bi}_2\text{O}_3@\text{TiO}_2$  compared to  $\text{TiO}_2$ , and the results are presented in Figure 4 and Table S1. As illustrated in Figure 4, the  $10\%$   $\text{Bi}_2\text{O}_3@\text{TiO}_2$  sample exhibits desorption peaks within the temperature ranges of  $200\text{--}300\text{ }^\circ\text{C}$ ,  $300\text{--}400\text{ }^\circ\text{C}$ , and  $500\text{--}600\text{ }^\circ\text{C}$ , indicative of medium and strong acid sites. In contrast,  $\text{TiO}_2$  displays a single desorption peak at  $200\text{--}300\text{ }^\circ\text{C}$ , corresponding to medium acid sites. The data indicate that  $10\%$   $\text{Bi}_2\text{O}_3@\text{TiO}_2$  has a significantly higher acid amount ( $0.167\text{ mmol NH}_3/\text{g}$ ) than  $\text{TiO}_2$  ( $0.091\text{ mmol NH}_3/\text{g}$ ), as determined by the integral areas of the  $\text{NH}_3$  desorption peaks. The substantial increase in surface acidity observed in  $10\%$   $\text{Bi}_2\text{O}_3@\text{TiO}_2$  can be attributed to the introduction of

additional defect sites created by the impregnation of Bi species into the TiO<sub>2</sub> structure. This impregnation process not only enhances the surface acidity but also facilitates the formation of hydroxyl groups through increased water adsorption on the surface [28]. Consequently, this improvement in surface acidity significantly boosts the photocatalytic activity of the 10% Bi<sub>2</sub>O<sub>3</sub>@TiO<sub>2</sub> photocatalyst.

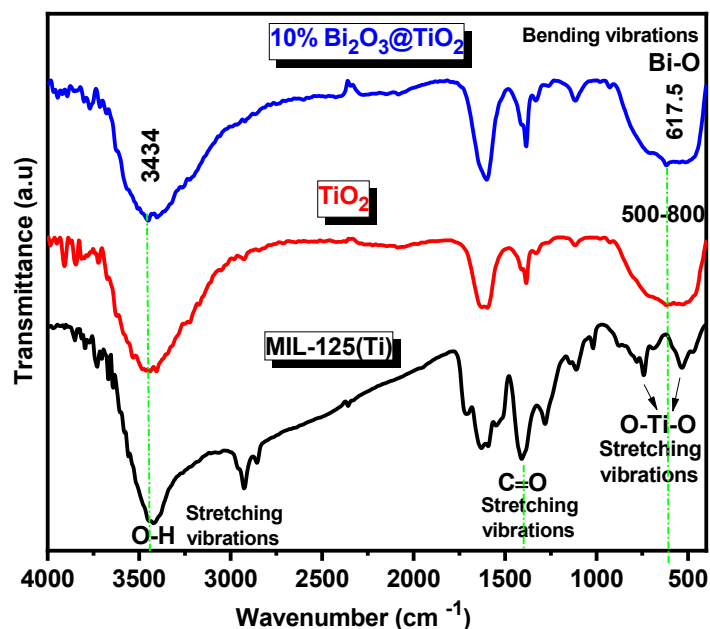


Figure 3. FT-IR spectra of various samples.

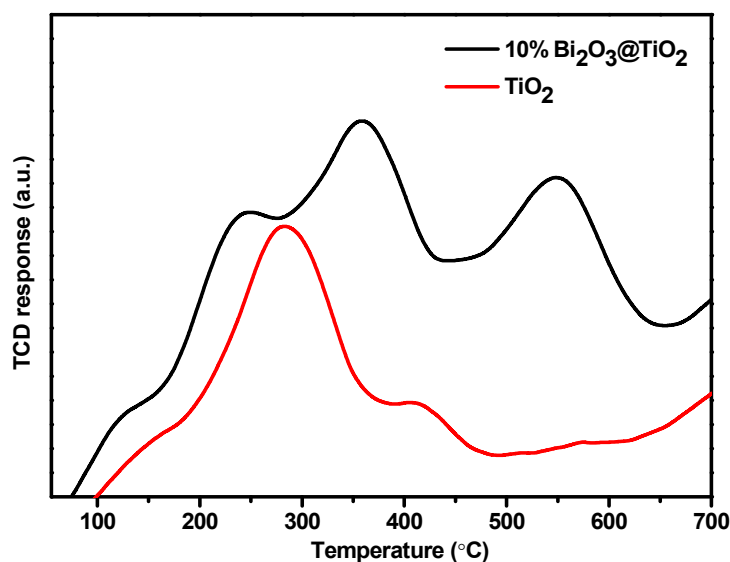
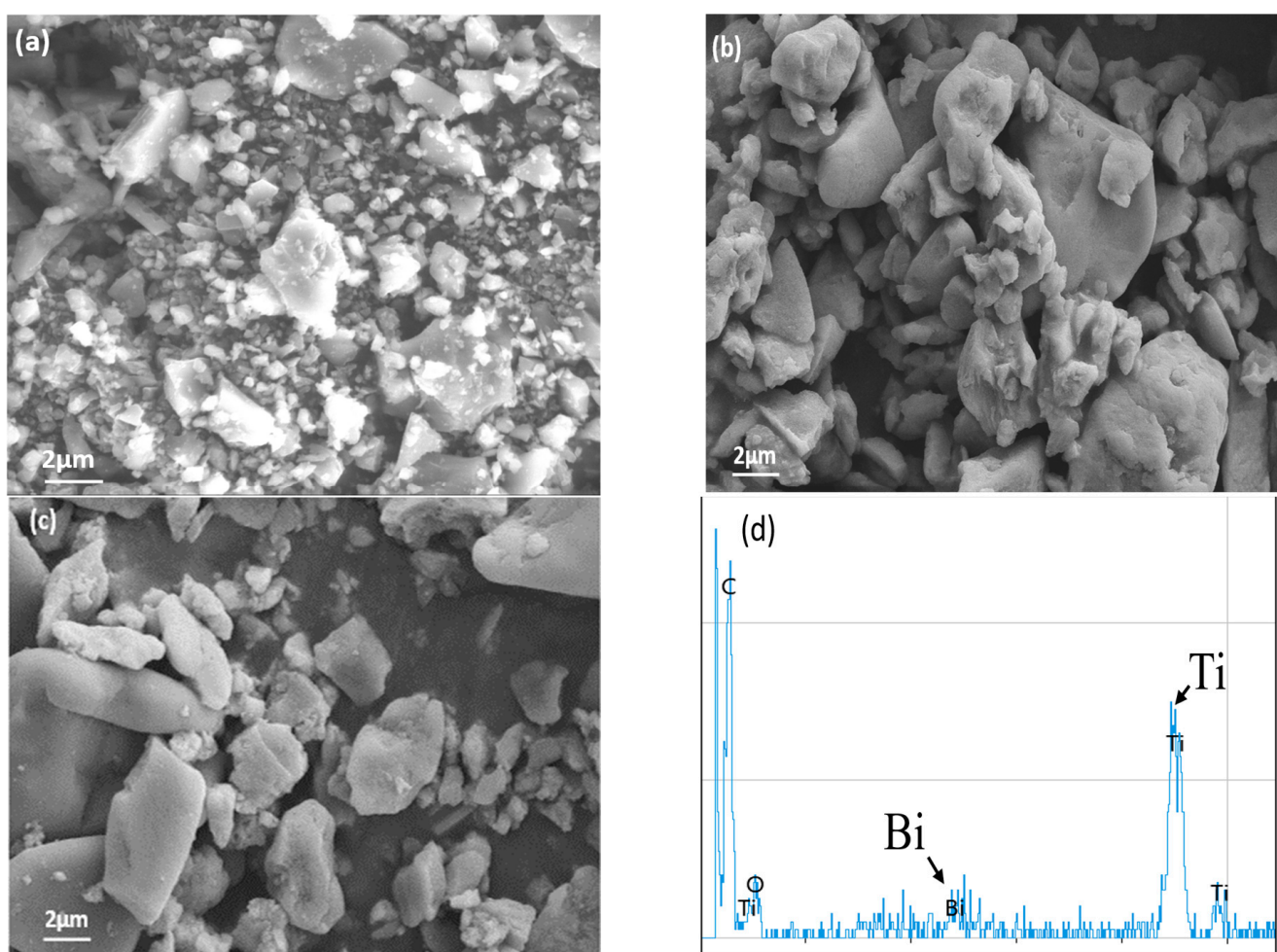


Figure 4. NH<sub>3</sub>-TPD profiles of TiO<sub>2</sub> and 10% Bi<sub>2</sub>O<sub>3</sub>@TiO<sub>2</sub>.

Figure 5 displays the SEM images of MIL125(Ti), TiO<sub>2</sub>, and 10% Bi<sub>2</sub>O<sub>3</sub>@TiO<sub>2</sub>. As seen, MIL125(Ti) possesses an irregular shape (Figure 5a), and TiO<sub>2</sub> exhibits a brick-like shape. Its average particle size is about 2 μm (Figure 5b). Comparatively, 10% Bi<sub>2</sub>O<sub>3</sub>@TiO<sub>2</sub> emerges in a distorted rhombus shape (Figure 5c). The average particle size is similar to that in TiO<sub>2</sub>. Further, the EDX image of 10% Bi<sub>2</sub>O<sub>3</sub>@TiO<sub>2</sub> reveals the existence of Bi species (Figure 5d). The Bi content in 10% Bi<sub>2</sub>O<sub>3</sub>@TiO<sub>2</sub> is 3.2%, which is close to the result from the XPS analysis.

To study the effect of the calcination temperature on the physicochemical properties of samples, N<sub>2</sub> adsorption desorption isotherms were measured (Figure 6a), and the textural

properties data are displayed in Table 1. The  $N_2$  sorption isotherm of MIL-125(Ti) is represented by the type I isotherm with an  $H_3$  hysteresis loop at  $P/P_0 > 0.4$ , which is a typical feature of microporous materials. A large specific surface area is found ( $891 \text{ m}^2 \text{ g}^{-1}$ ). When MIL-125(Ti) is calcined at high temperature ( $500 \text{ }^\circ\text{C}$ ), type IV isotherms with an  $H_2$  hysteresis loop at  $P/P_0 > 0.6$  are observed on the  $\text{TiO}_2$  and  $10\% \text{ Bi}_2\text{O}_3@/\text{TiO}_2$  samples due to the presence of mesopores. Compared with MIL-125(Ti), the specific surface areas (BET) of  $\text{TiO}_2$  and  $10\% \text{ Bi}_2\text{O}_3@/\text{TiO}_2$  after calcination become  $93 \text{ m}^2 \text{ g}^{-1}$  and  $164 \text{ m}^2 \text{ g}^{-1}$ , respectively. This is attributed to the disappearance of many micropores and the development of new mesopores during the collapse of the MOF network in the calcination process [29]. Figure S1 shows the pore size distribution of different samples. Additionally, the particles size distribution of  $10\% \text{ Bi}_2\text{O}_3@/\text{TiO}_2$  is exhibited in the captured TEM image (Figure 6b), in which their irregular shape along with the average particle size around  $\sim 200 \text{ nm}$  can be observed.



**Figure 5.** SEM images of (a) MIL-125(Ti), (b)  $\text{TiO}_2$ , and (c)  $10\% \text{ Bi}_2\text{O}_3@/\text{TiO}_2$  and (d) EDX image of  $10\% \text{ Bi}_2\text{O}_3@/\text{TiO}_2$ .

**Table 1.** Physicochemical parameters of MIL-125,  $\text{TiO}_2$ , and  $10\% \text{ Bi}_2\text{O}_3@/\text{TiO}_2$ .

Sample	BET Surface Area ( $\text{m}^2 \text{ g}^{-1}$ )	Pore Volume ( $\text{cm}^3/\text{g}$ )	Pore Diameter (nm)
MIL-125(Ti)	891.7	0.25	1.79
$\text{TiO}_2$	93	0.25	6.7
$10\% \text{ Bi}_2\text{O}_3@/\text{TiO}_2$	164	0.48	8.12

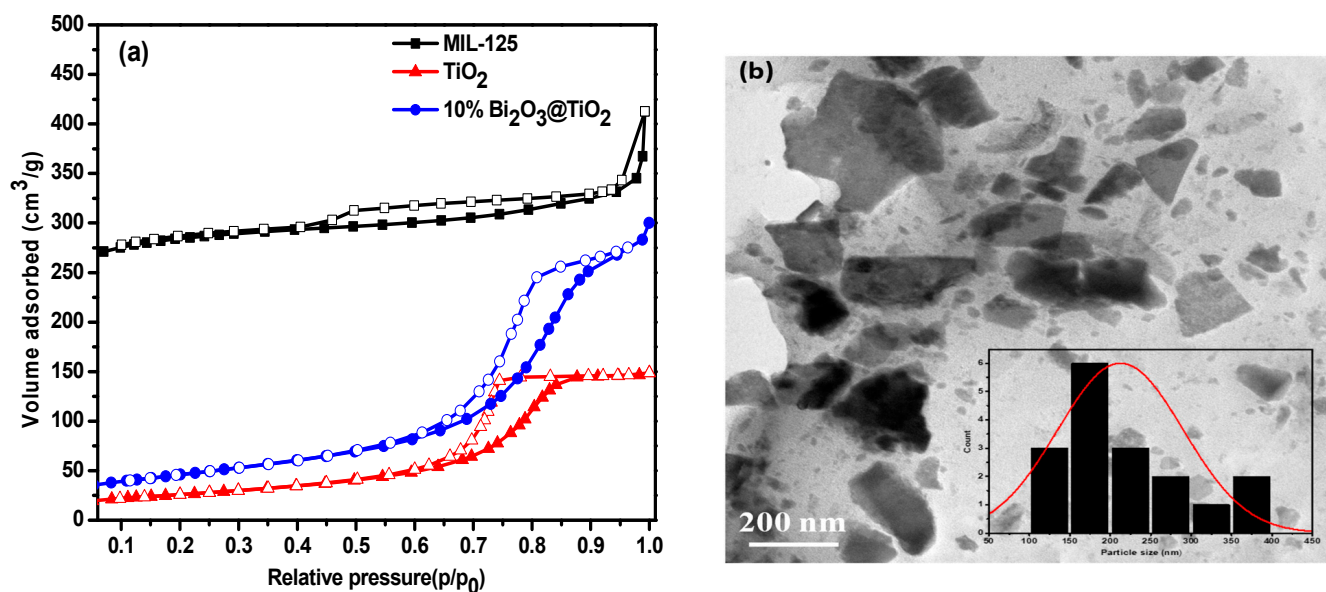


**Figure 6.** (a) N<sub>2</sub> adsorption/desorption isotherms of samples, (b) TEM image, and particle size distribution (inset figure) of 10% Bi<sub>2</sub>O<sub>3</sub>@TiO<sub>2</sub>.

## 2.2. Photocatalytic Degradation of EBT Dye

The photocatalytic activity of various samples was further investigated through the photocatalytic degradation of EBT. Moreover, the effect of some factors such as the irradiation time, the photocatalyst dosage, the initial concentration of dye, and pH on the photocatalytic degradation was studied.

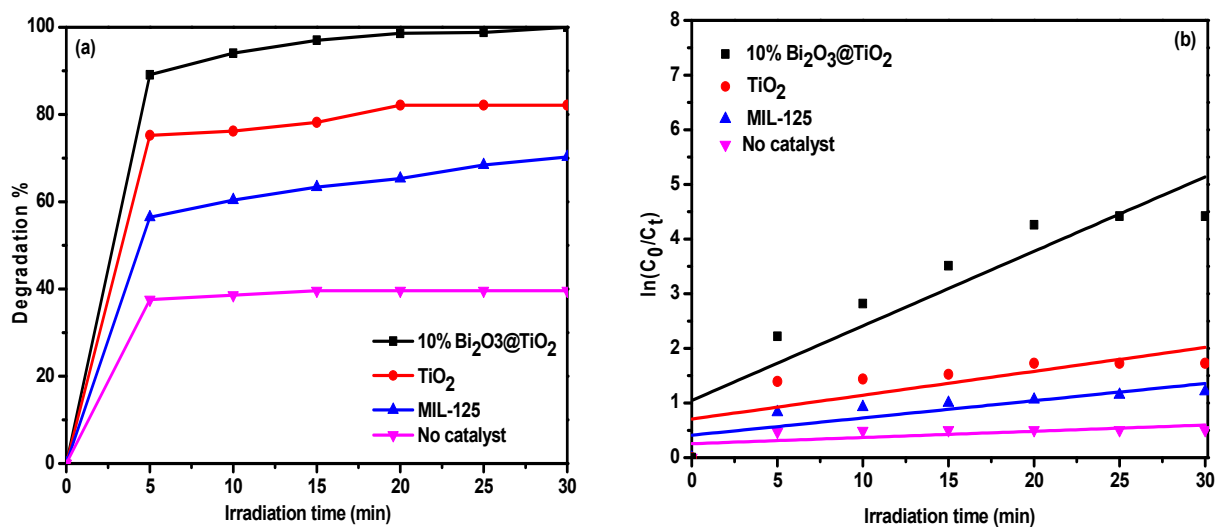
### 2.2.1. Effect of Irradiation Time

The effect of irradiation time was first studied for 30 min at time intervals of 5 min as shown in Figure 7a. MIL-125 showed the least activity for the EBT degradation, whereas TiO<sub>2</sub> exhibited good photocatalytic performance, and the enhanced photocatalytic efficiency of EBT was observed over the 10% Bi<sub>2</sub>O<sub>3</sub>@TiO<sub>2</sub> composite (70.3%, 82.16%, and 100% degradation, respectively). The photocatalytic degradation of EBT follows the pseudo-first order reaction kinetic ( $-\ln(C_t/C_0) = kt$ ) as shown in Figure 7b. The reaction rate was calculated by the apparent reaction rate constant ( $k$ ) from the degradation curves of  $\ln(C_0/C_t)$  versus the irradiation time. The reaction rates of the various samples were in the following order: MIL-125 < TiO<sub>2</sub> < 10% Bi<sub>2</sub>O<sub>3</sub>@TiO<sub>2</sub>. The  $k$  value of 10% Bi<sub>2</sub>O<sub>3</sub>@TiO<sub>2</sub> (0.212 min<sup>-1</sup>) is 4.85-fold that of TiO<sub>2</sub> (0.0437 min<sup>-1</sup>) and 6.63-fold that of MIL-125 (0.032 min<sup>-1</sup>), indicating that the photocatalytic degradation was enhanced by applying the mixed oxides. Therefore, the 10% Bi<sub>2</sub>O<sub>3</sub>@TiO<sub>2</sub> was employed to further investigate the optimum parameters for the photocatalytic degradation in the following work.

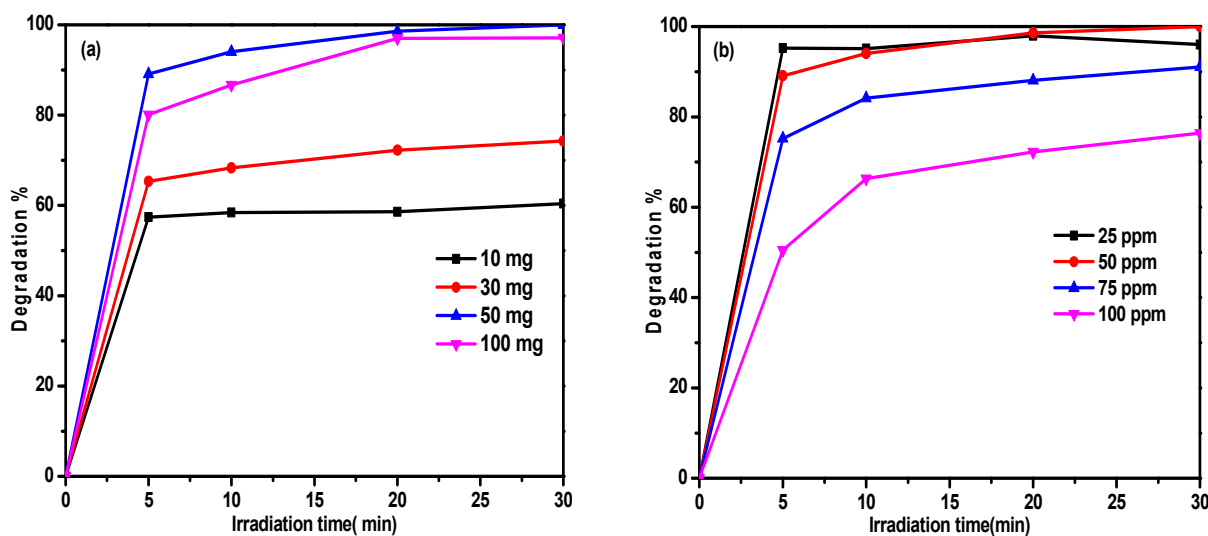
### 2.2.2. The Dosage Effect of the Photocatalyst and Dye Concentration

Figure 8a shows the influence of the catalyst dose on the photocatalytic degradation of EBT assessed at pH = 6, 50 ppm EBT solution. It was observed that the degradation percent (%) increased by increasing the photocatalyst dosage due to the increase in the number of active sites and the number of free radicals ( $\cdot\text{OH}$  and  $\text{O}_2^{\cdot-}$ ) [30]. The optimum dosage was 50 mg. When the catalyst dosage was further increased beyond the optimum dosage, the percent degradation was decreased; this may be because when the dosage increases, the suspended particles of the photocatalyst accumulate together, which inhibits the amount of irradiation light that reaches the active sites, and consequently, the rate of degradation was decreased [31]. Additionally, the effect of the concentration of EBT dye was assessed (50 mg catalyst dose, pH = 6) as presented in Figure 8b. The degradation efficiency decreased to 76% with an increase in the concentration of dye to 100 ppm. When the concentration of

dye increases, the molecules of dye accumulate on the surface of the catalyst and block the active sites, so the penetration of light to the catalyst decreases, which in turn decreases the degradation efficiency [32].



**Figure 7.** (a) Degradation performance of EBT (50 mL, 50 ppm) with 50 mg of various prepared samples. (b) Plot of  $\ln(C_0/C_t)$  as a function of irradiation time.



**Figure 8.** The effect of the catalyst dose of 10% Bi<sub>2</sub>O<sub>3</sub>@TiO<sub>2</sub> as a photocatalyst (a), and the effect of different concentrations on the degradation of EBT dye (b).

### 2.2.3. Effect of pH

The pH level is a critical factor in photocatalytic degradation, and its impact was studied on 10% Bi<sub>2</sub>O<sub>3</sub>@TiO<sub>2</sub> and TiO<sub>2</sub> catalysts (Figure 9). To confirm the role of Bi<sup>3+</sup> in enhancing the degradation efficiency, we compared the performance of both catalysts under varying pH conditions (Figure 9). At low pH levels, the anionic nature of EBT predominated, resulting in a positively charged photocatalyst surface that enhanced dye adsorption. While TiO<sub>2</sub> showed no significant effect at high pH (pH = 10), 10% Bi<sub>2</sub>O<sub>3</sub>@TiO<sub>2</sub> demonstrated a 68% degradation of EBT dye under the same conditions, confirming that Bi<sup>3+</sup> impregnation enhances the catalytic efficiency of TiO<sub>2</sub>. This improvement is attributed to Bi<sup>3+</sup> attracting more water molecules due to its higher acidity as elucidated by NH<sub>3</sub>-TPD. The higher adsorption of water molecules onto the 10% Bi<sub>2</sub>O<sub>3</sub>@TiO<sub>2</sub> surface during light irradiation enhances the formation of hydroxyl groups that act as electron pair donors, with



hole-induced oxidation reactions converting them into  $\cdot\text{OH}$  free radicals, which are highly effective in promoting dye degradation [28]. Our findings indicate that an acidic medium is optimal for EBT degradation. In control experiments without 10%  $\text{Bi}_2\text{O}_3@\text{TiO}_2$  at pH = 3 and 50 ppm initial dye concentration, only 60% degradation of EBT was observed after 30 min, demonstrating that complete degradation does not occur without a photocatalyst under light irradiation.

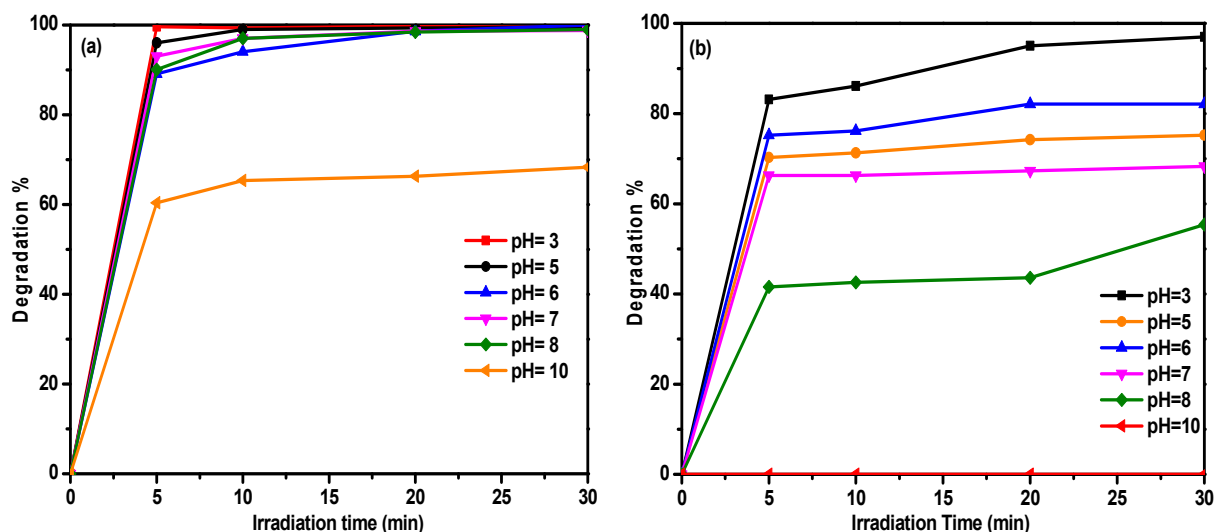


**Figure 9.** Effect of pH on the photodegradation of EBT by using 50 mg of (a) 10%  $\text{Bi}_2\text{O}_3@\text{TiO}_2$  and (b)  $\text{TiO}_2$ .

Furthermore, when comparing the photocatalytic activity of 10%  $\text{Bi}_2\text{O}_3@\text{TiO}_2$  with other photocatalysts for EBT degradation (Table 2), it was evident that 10%  $\text{Bi}_2\text{O}_3@\text{TiO}_2$  exhibited superior degradation performance under low light energy and shorter reaction times.

**Table 2.** Comparison of the photocatalytic degradation of EBT with different catalysts.

Entry	Catalyst	Light Source	Time	Degradation (%)	Ref.
1	$\text{CdS}/\text{BiVO}_4$	40 WATT Tungsten lamp	30 min	64%	[33]
2	$\text{SnO}_2$ nanoparticles	500 WATT Mercury vapor lamp	4.5 h	77%	[34]
3	$\text{BaWO}_4/\text{MoS}_2$	UV illumination	60 min	99.2%	[35]
4	$\text{TiO}_2/g\text{-C}_3\text{N}_4$	UV light	3 h	100%	[36]
5	Mf-NGr-CNTs- $\text{SnO}_2$ heterostructures	Sun light	2 h	82%	[37]
6	$\text{SnO}_2/\text{ZnO}$ nanocomposite	Solar light	3 h	98%	[38]
7	$\text{NiO-ZnO}$	UV light	90 min	80%	[39]
8	10% $\text{Bi}_2\text{O}_3@\text{TiO}_2$	200 WATT Tungsten lamp	30 min	100%	This work

### 2.3. UV-Vis Diffuse Reflectance Spectra of Catalysts

UV-Vis diffuse reflectance spectra (UV-DRS) is a technique used to characterize the optical properties of materials by measuring the amount of light reflected at different wavelengths. In the context of materials such as MIL-125,  $\text{TiO}_2$ , and 10% $\text{Bi}_2\text{O}_3@\text{TiO}_2$ , UV-DRS provides valuable information about their absorption and reflectance properties in the ultraviolet–visible (UV-Vis) range. Figure 10 shows the UV-Vis diffuse reflectance spectra of MIL-125,  $\text{TiO}_2$ , and 10%  $\text{Bi}_2\text{O}_3@\text{TiO}_2$ . From Figure 10, it can be observed that

the UV-DRS spectrum of TiO<sub>2</sub> exhibits the highest absorbance compared to the other two materials. This suggests that TiO<sub>2</sub> has a higher tendency to absorb light in the UV-Vis range. While the UV-DRS spectrum of 10% Bi<sub>2</sub>O<sub>3</sub>@TiO<sub>2</sub> is located between MIL-125 and TiO<sub>2</sub> in terms of absorbance, 10% Bi<sub>2</sub>O<sub>3</sub>@TiO<sub>2</sub> shows moderate absorbance across the measured wavelengths, indicating its ability to absorb light in the UV-Vis range, albeit to a lesser extent than TiO<sub>2</sub>. On the other hand, the UV-DRS spectrum of MIL-125 appears to have the lowest absorbance among the three materials. This suggests that the incorporation of bismuth into MIL-125 by impregnation/calcination methods has enhanced its light absorption capabilities in the UV-Vis range. Additionally, the UV-DRS spectrum of 10% Bi<sub>2</sub>O<sub>3</sub>@TiO<sub>2</sub> would exhibit features that arise from the combined effects of TiO<sub>2</sub> and bismuth oxide, providing insights into their synergistic behavior and potential applications in photocatalysis. From the UV-vis DRS spectra, the bandgap energy of the constructed photocatalysts was calculated (Equation (1)) based on the Tauc's plots [40], as shown in the inset of Figure 10:

$$(\alpha h\nu)^n = K(h\nu - E_g) \quad (1)$$

where  $\alpha$  is the absorption coefficient,  $h\nu$  is the photon energy,  $n = 2$  or  $\frac{1}{2}$  for direct or indirect transition,  $K$  is the absorption constant, and  $E_g$  is the bandgap energy (eV).

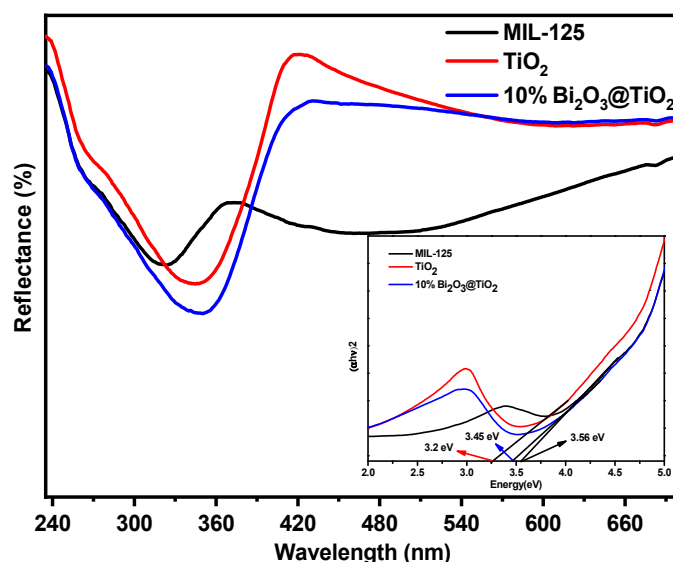


**Figure 10.** UV-Vis DRS of MIL125 (Ti), TiO<sub>2</sub>, and 10% Bi<sub>2</sub>O<sub>3</sub>@TiO<sub>2</sub> and the plots of  $(\alpha h\nu)^2$  versus energy ( $h\nu$ ) (inset).

#### 2.4. Optimized Geometry and Electrical Features of EBT

Figure 11 shows The structure of Eriochrome Black T dye (EBT) with the standard color of atoms and their numerical order used in DFT and TD-DFT calculations. The optimized structures and FMO amplitudes for neutral EBT and the protonated forms (HEB<sup>-2</sup>(O24) and EB<sup>-3</sup>) are shown in Figure 12. The EBT dye's LUMO and HOMO electron densities are plainly spread over some atoms in the compounds. This is found for EBT in the neutral and protonated forms; the LUMO is placed on the nitro group with the values of  $-3.432$  eV,  $-3.154$  eV,  $-3.085$  eV,  $-2.925$  eV, and  $-2.831$  eV for neutral EBT and protonated forms, respectively, as exhibited in Table 2, while the HOMO densities are located on the carbon atoms of the naphthalene ring (C1, C2, C3, C4, C7, C8, C9, C10) and the hydroxyl groups with values of  $-5.877$  eV,  $-5.818$  eV,  $-5.080$  eV,  $-5.314$  eV, and  $-4.670$  eV for neutral EBT and protonated forms, respectively (Table 3). The HOMO and LUMO energies ( $E_{HOMO}$ ,  $E_{LUMO}$ ) help assess the molecules' ability to donate or accept electrons [41]. Moreover, the lowest  $\Delta E_{\text{gap}}$  values of EB<sup>-3</sup> and HEB<sup>-2</sup>(O24) indicate the highest chemical reactivity compared to other species [42]. Additionally, the remaining protonated forms of dye (H<sub>2</sub>EB<sup>-</sup> and HEB<sup>-2</sup>(O25)) show the same behavior as shown in Figure S4.

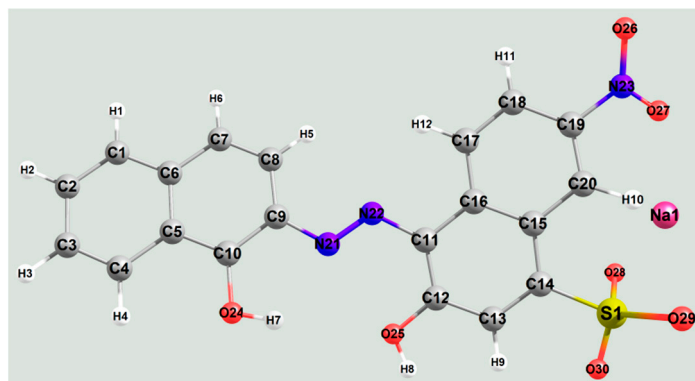


**Figure 11.** The structure of Eriochrome Black T dye (EBT), carbon atoms (grey), nitrogen atoms (blue), oxygen atoms (red), hydrogen atoms (white), sodium atoms (pink), and sulfur atom (yellow).

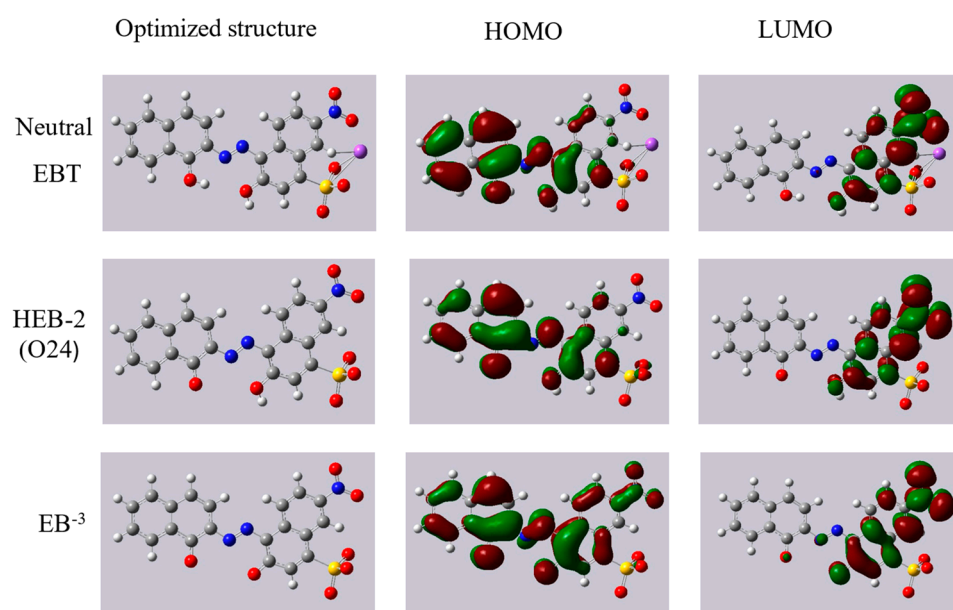


**Figure 12.** The optimized structures and FMO amplitudes (LUMO and HOMO electron densities) for neutral EBT and protonated forms calculated at B3LYP/6-311++G(d,p) level in water.

**Table 3.** Calculated HOMO energies (EHOMO), LUMO energies (ELUMO), HOMO–LUMO energy gap (Eg) in eV, and charge transfer N (e) of systems.

System	$E_{\text{tot}}$ (eV $\times 10^4$ )	$E_{\text{HOMO}}$ (eV)	$E_{\text{LUMO}}$ (eV)	$\Delta E_{\text{gap}}$ (eV)	N (eV)
Neutral EBT	−5.498	−5.877	−3.432	2.444	0.113
H <sub>2</sub> EB <sup>−</sup>	−5.057	−5.818	−3.154	2.664	0.132
HEB <sup>2−</sup> (O24)	−5.056	−5.080	−3.085	1.994	0.120
HEB <sup>−2</sup> (O25)	−5.056	−5.314	−2.925	2.389	0.141
EB <sup>−3</sup>	−5.055	−4.670	−2.831	1.838	0.131

Further, Table 4 represents the electronic properties (IP, EA,  $\mu$ ,  $\eta$ ,  $\sigma$ ,  $\chi$ ,  $\omega$ , and S) for neutral EBT and its protonated forms that were calculated at the B3LYP/6-311++G(d,p) level in water. The data suggests that HEB<sup>−2</sup>(O24) and EB<sup>−3</sup> are the most chemically reactive forms. Overall, these findings indicate that EB<sup>−3</sup> and HEB<sup>−2</sup>(O24) are the most effective in the degradation process in aqueous environments, aligning well with experimental results. This confirms the computational study's agreement with practical observations.

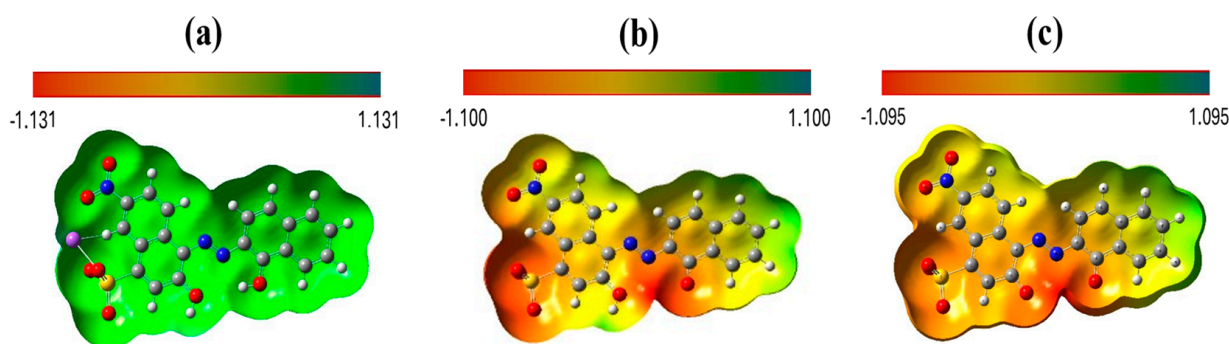
**Table 4.** Electronic properties of neutral EBT and protonated forms calculated at B3LYP/6-311++G(d,p) level in water.

System	IP (eV)	EA (eV)	X (eV)	$\mu$ (eV)	$\eta$ (eV)	S (eV)	$\omega$ (eV)	$\mu$ (Debye)
Neutral EBT	5.877	3.432	4.654	−4.654	1.222	0.409	8.861	10.842
H <sub>2</sub> EB <sup>−</sup>	5.818	3.154	4.486	−4.486	1.332	0.375	7.553	32.023
HEB <sup>2−</sup> (O24)	5.080	3.085	4.083	−4.083	0.997	0.501	8.356	21.549
HEB <sup>−2</sup> (O25)	5.314	2.925	4.120	−4.120	1.195	0.419	7.103	35.218
EB <sup>−3</sup>	4.670	2.831	3.750	−3.750	0.919	0.544	7.648	26.997

### 2.5. Mulliken Atomic Charges and ESP

Mulliken atomic charges are essential in quantum chemistry, influencing molecular properties such as the electronic structure, polarization, and dipole moments. These charges provide insight into the electron distribution within molecules and are key in predicting chemical reactions [43–45]. In a study using the DFT method with the 6-311++G(d,p) basis set, the Mulliken charges were calculated to pinpoint the degradation centers in neutral EBT dyes and their protonated forms. The findings revealed that oxygen and nitrogen atoms, with higher negative charges (Table S2), play a significant role in interacting with a 10% Bi<sub>2</sub>O<sub>3</sub>@TiO<sub>2</sub> photocatalyst, driving dye degradation. Additionally, specific carbon atoms (C9, C10, C11, C12, C19) and hydrogen atoms (H8 and H7) in the hydroxyl group show varying charges, which affect their roles in the degradation process. Moreover, the highest negative charges are found on O28 and O29 in the sulfonyl groups, attributed to their proximity to sulfur atoms.

Electrostatic potential (ESP) is a fundamental property used to evaluate the charge distribution in a molecule, providing insights into its reactivity and interactions with other species. By calculating the ESP based on the electron density distribution obtained from quantum chemical calculations, we can understand the distribution of positive and negative charges within Eriochrome Black T dye. Analyzing the ESP helps in studying the adsorption and degradation processes of the dye over the 10% Bi<sub>2</sub>O<sub>3</sub>@TiO<sub>2</sub> catalyst. Figure 13 shows the ESP maps for neutral EBT and the protonated forms (HEB<sup>−2</sup>(O24) and EB<sup>−3</sup>) that visualize regions of high and low electron density, where high negative values correspond to negatively charged areas and high positive values indicate positively charged areas. These regions represent reactive centers or potential interaction sites with other molecules or catalyst surfaces. Oxygen, nitrogen, and specific carbon atoms play significant roles in Eriochrome Black T dye's reactivity. Hydroxyl, nitro, and sulfuric groups associated with oxygen atoms exhibit high ESP values, suggesting their involvement in the adsorption process and potential interactions with the 10% Bi<sub>2</sub>O<sub>3</sub>@TiO<sub>2</sub> photocatalyst, leading to degradation pathways. The ESP maps of the rest of the forms of dye (H<sub>2</sub>EB<sup>−</sup> and HEB<sup>−2</sup>(O25)) are mentioned in Figure S3.

**Figure 13.** Contour representations of the electrostatic potential regions of negative (positive) potential shown in red (green) for molecules: (a) neutral EBT, (b) HEB<sup>−2</sup>(O24), and (c) EB<sup>−3</sup> in the aqueous phase using the B3LYP/6-311++G(d,p) method.

## 2.6. UV-Vis Absorption Spectra

Time-Dependent Density Functional Theory (TD-DFT) is a computational method widely used to simulate UV-Vis absorption spectra for molecules such as Eriochrome Black T dye. It provides information about the molecule's electron distribution and energy levels. By promoting electrons from occupied orbitals (HOMO) to unoccupied orbitals (LUMO) using time-dependent perturbation theory, excited states are determined. TD-DFT calculations are performed to simulate the UV-Vis absorption spectra of Eriochrome Black T dye, revealing the wavelengths ( $\lambda$ ) at which electronic transitions occur, indicating the absorption of light at specific energy levels. The maximum wavelength ( $\lambda_{max}$ ) corresponds to the HOMO–LUMO transition, which governs the main absorption peak. Comparing the simulated UV-Vis absorption spectra with experimental data validates and verifies the theoretical results. In the case of Eriochrome Black T dye, the calculated  $\lambda_{max}$  values for  $\text{HEB}^{-2}$  (O24) and  $\text{EB}^{-3}$  (519 nm and 529 nm) (Figure 14a) closely match the experimental value (532 nm) (Figure 14b). This suggests that the anionic  $\text{HEB}^{-2}$  (O24) or  $\text{EB}^{-3}$  forms of the dye could potentially undergo degradation processes.

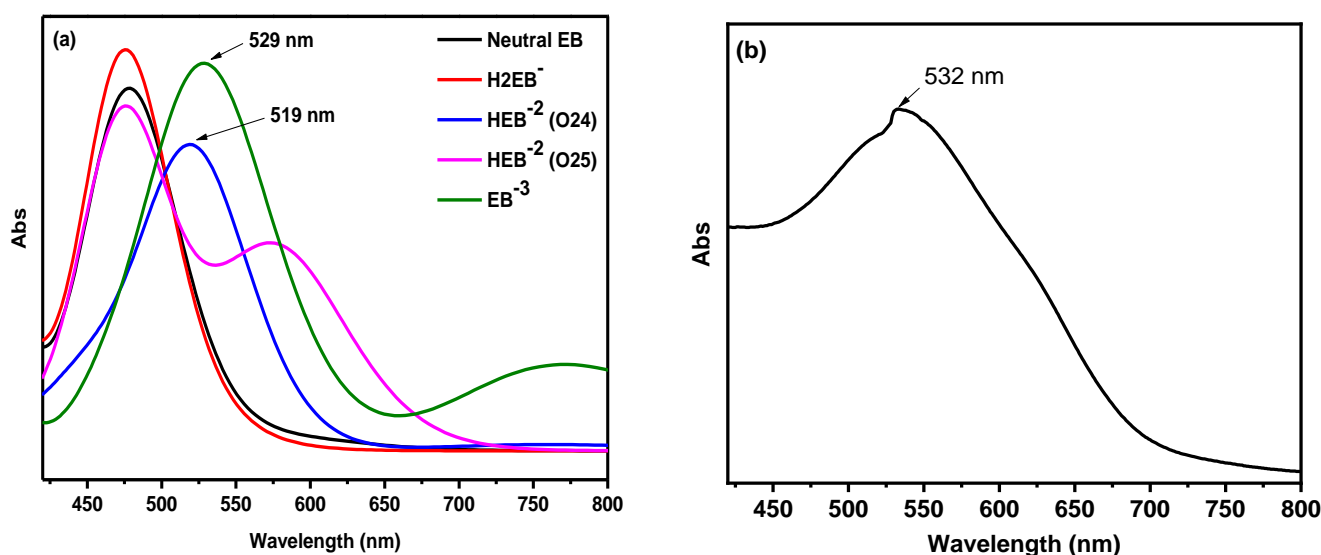
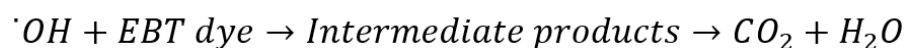
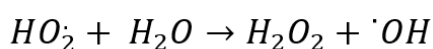
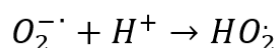
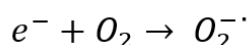
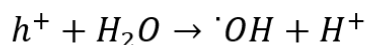
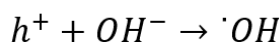
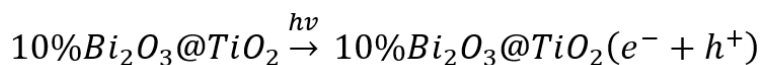


**Figure 14.** (a) The simulated UV-Vis absorption spectra of dye (neutral EBT and protonated forms) by using time-dependent DFT (TD-DFT) method. (b) The experimental absorption spectra of EBT dye solution.

## 2.7. Photocatalytic Degradation Mechanism of EBT over 10% Bi<sub>2</sub>O<sub>3</sub>@TiO<sub>2</sub>

Based on both practical and theoretical studies of EBT degradation, proposed mechanisms can be formulated to illustrate how EBT dyes degrade on the surface of the 10% Bi<sub>2</sub>O<sub>3</sub>@TiO<sub>2</sub> photocatalyst. As shown in Scheme 1 10% Bi<sub>2</sub>O<sub>3</sub>@TiO<sub>2</sub> was exposed to light radiation, which energized the existing electrons and moved them from the valence band (VB) to the conduction band (CB). As a result, strongly oxidizing reactive positive holes (h<sup>+</sup>) were produced in the VB, which in turn react with H<sub>2</sub>O leading to the generation of radical hydroxide (•OH). In contrast, electrons in the photocatalyst CB possess a significant reducing ability and can react with O<sub>2</sub> and •OH to produce superoxide ion (O<sub>2</sub><sup>-•</sup>). The generated reactive species (•OH) and (O<sub>2</sub><sup>-•</sup>) react with EBT dye adsorbed on the photocatalyst surface leading to their degradation. The degradation of products further undergoes reactions with reactive species, resulting in the mineralization of the dye molecules into simpler, less harmful compounds, such as CO<sub>2</sub> and water, as suggested in the following:



**Scheme 1.** The suggested mechanism of EBT degradation over 10%Bi<sub>2</sub>O<sub>3</sub>@TiO<sub>2</sub> photocatalyst.

### 2.8. Photocatalytic Activity Towards Different Substrates

The as-prepared photocatalyst (10% Bi<sub>2</sub>O<sub>3</sub>@TiO<sub>2</sub>) showed observable activity towards another anionic dye, Congo Red (CR), as well as cationic dyes such as Malachite Green (MG), Methylene Blue (MB), and Safranin O (SO) as shown in Figure 15. A total of 50 mg of photocatalyst was added to 10 ppm of each dye solution and stirred for 30 min in the dark before visible light irradiation, and the photocatalytic efficiency percent was calculated from Equation (2)

$$\text{Photocatalytic efficiency \%} = \frac{A_0 - A_t}{A_0} \times 100 \quad (2)$$

where A<sub>0</sub> is the absorbance of the initial concentration of dye solution (10 ppm) and A<sub>t</sub> is the absorbance after time. Figure 15 shows that 99% of the CR dye was decomposed after only 15 min of visible light irradiation at pH = 3. This could be due to its anionic nature, which is similar to that of EBT dye. The degradation of the other cationic dyes MG, MB, and SO was performed at pH = 9.5, and after 30 min of light irradiation, it was found that 95% and 81% of MG and MB were degraded, respectively, but only 68% of SO was degraded due to the strong stability. The effective activity of 10% Bi<sub>2</sub>O<sub>3</sub>@TiO<sub>2</sub> towards these different types of dyes reveals its amphoteric and pH-dependent photocatalytic nature [46]. Figure S4 shows the percent degradation of the four dyes. In addition to the colored dyes, the photocatalytic activity of 10% Bi<sub>2</sub>O<sub>3</sub>@TiO<sub>2</sub> was investigated for the degradation of lidocaine hydrochloride (LDC), a commonly used local anesthetic and antiarrhythmic agent. Due to its high polarity and low Henry's coefficient, LDC easily enters water systems and is not fully removed by conventional sewage treatments, highlighting the need for more effective removal methods [47]. In this study, 50 mg of 10% Bi<sub>2</sub>O<sub>3</sub>@TiO<sub>2</sub> was added to a 50 ppm LDC solution and stirred in the dark for 30 min before exposure to visible light. As shown in Figure S6, the peak absorbance of the LDC solution increased post-degradation, likely due to the intermediate by-products with strong UV-Vis spectra [48]. These by-products, such as 2,6-dimethylaniline, contain conjugated or hydroxylated structures that absorb more UV light. This temporary increase in absorbance occurs before full mineralization reduces the solution to baseline levels [49]. These findings confirmed the efficiency of prepared catalysts toward different materials.

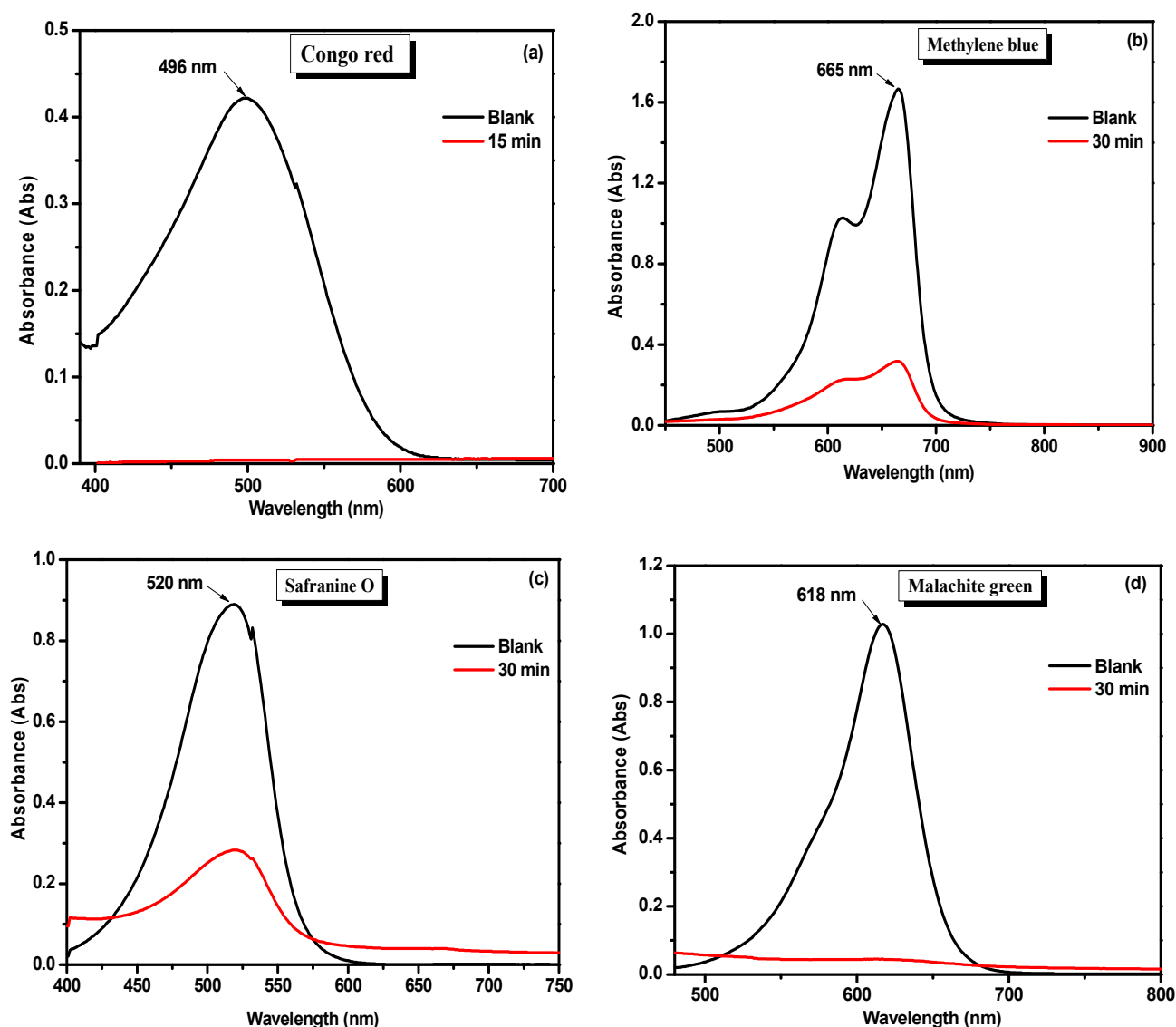


**Figure 15.** Decomposition of (a) CR dye (0.05 g catalyst, 10 ppm 50 mL dye solution, pH = 3, 15 min irradiation time). (b–d) MB, SO, and MG dyes, respectively, (0.05 g catalyst, 10 PPM 50 mL dye solution, pH = 9.5, 30 min irradiation time) using synthesized 10% Bi<sub>2</sub>O<sub>3</sub>@TiO<sub>2</sub>.

### 2.9. Reusability Test

A cycle experiment was conducted on 10% Bi<sub>2</sub>O<sub>3</sub>@TiO<sub>2</sub> to evaluate its reusability (Figure 16a). After every cycle, the catalyst was separated by centrifugation and added to a fresh dye solution without regeneration. Notably, even after four cycles, the yield remained at 76%. The XRD study was also performed on the spent catalyst to determine its structural stability after recycling. The structure of 10% Bi<sub>2</sub>O<sub>3</sub>@TiO<sub>2</sub> was maintained after four cycles, according to the XRD results of the samples after the reusability (Figure 16b), which shows that the structure of 10% Bi<sub>2</sub>O<sub>3</sub>@TiO<sub>2</sub> is stable during the photocatalytic degradation reaction. Additionally, the reusability test with regeneration of the catalyst shows reduced deterioration findings after four cycles (Figure S7). This could be attributed to the leaching of the catalyst into the washer liquor. This demonstrates that the catalyst is more affordable and environmentally beneficial.

The above results reveal the novelty of this study through producing recyclable and efficient photocatalysts sensitive to visible light and able to degrade both anionic and cationic dyes in a short time.

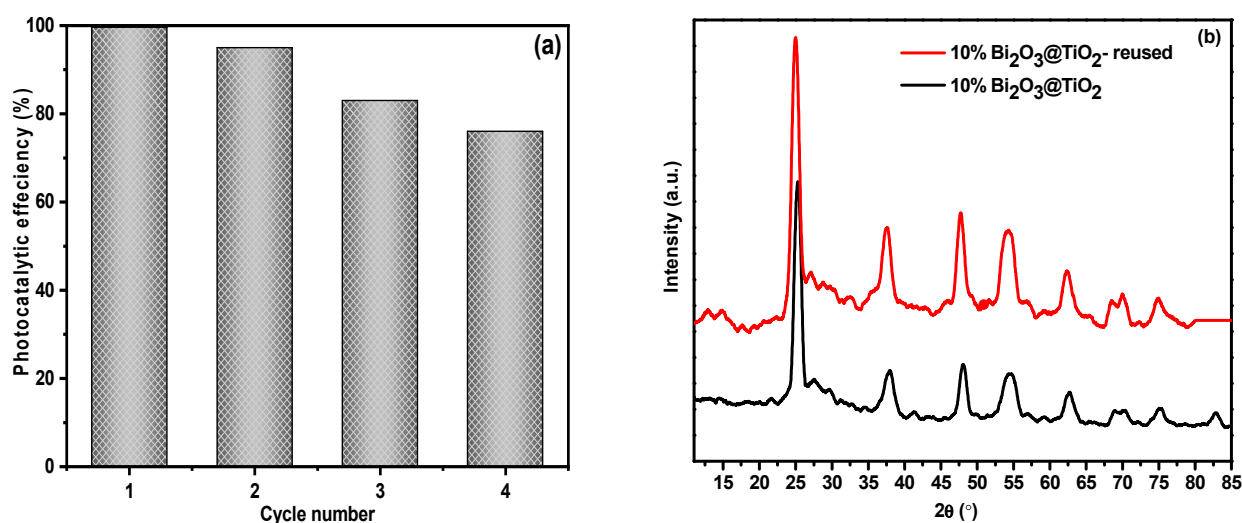


**Figure 16.** (a) The cycling runs of the degradation of EBT dye over 10%  $\text{Bi}_2\text{O}_3@\text{TiO}_2$ . (b) XRD patterns of the spent catalyst.

### 3. Experimental Details

#### 3.1. Materials

Titanium (IV) isopropoxide (TTIP, 97%, Sinopharm, Shanghai, China), 1,4-benzenedicarboxylic acid (BDC, 98%, LOBA CHEMIE, Mumbai, India), Bismuth (III) nitrate pentahydrate (98%, Sinopharm, China), Ammonium sulfide solution, Dimethyl formamide (DMF, 98%, Sinopharm, China), Ethanol (99%, Sinopharm, China), Methanol (99.8%, Sinopharm, China), Acetone (99%, Sinopharm, China), Eriochrome Black T (99%, LOBA CHEMIE, India), Congo Red (99%, LOBA CHEMIE, India), Malachite Green (99%, LOBA CHEMIE, India), Methylene Blue (99%, LOBA CHEMIE, India), Safranin O (99%, LOBA CHEMIE, India), HCl (37%, Sinopharm, China), and NaOH (99%, LOBA CHEMIE, India) were used directly without any further purification.

#### 3.2. Synthesis Procedures

##### 3.2.1. Synthesis of Ti-MOF

MIL-125 was solvothermal constructed from 250 mg of 1.5 mmol 1,4-benzenedicarboxylic acid (BDC) and titanium (IV) isopropoxide  $\text{Ti}(\text{OiPr})_4$  (0.3 mL, 1 mmol) introduced into a solution of 4.5 mL of N, N-dimethylformamide (DMF) and 500  $\mu\text{L}$  of dry methanol [26,50]. The mixture was stirred softly for 30 min at room temperature and then introduced to a 25 mL Teflon-lined autoclave at 150 °C for 15 h. The mixture was left to cool down to room temperature, and then the white solid was collected via centrifugation, washed twice with acetone, dried overnight at 100 °C, and then dried under vacuum at 150 °C for 24 h.

##### 3.2.2. Synthesis of Mixed Oxide $\text{Bi}_2\text{O}_3@\text{TiO}_2$

Certain amounts of Ti-MOF were sonicated in distilled water for 15 min to form a pale yellow suspension. Then, the calculated percentage of bismuth (III) nitrate pentahydrate (10, 20, and 30 wt.% based of the MOF weight) was dispersed in distilled water and added to a Ti-MOF suspension with stirring for 30 min. After that, ammonium sulfide solution was gently added dropwise as a precipitating agent, and the mixture turned into a brown color that was still stirred at 80 °C for 2 h. The brown precipitate was collected by centrifugation and then washed twice with distilled water and acetone. After that, the brown precipitate was dried overnight at 60 °C to obtain a brown powder that was calcined at 500 °C for 2 h to obtain a pale-yellow powder of mixed oxides. The final products were specified as 10%, 20%, and 30%  $\text{Bi}_2\text{O}_3@\text{TiO}_2$  according to the weight percent of bismuth (III) nitrate pentahydrate. Additionally, the prepared Ti-MOF was calcined at 500 °C for 2 h to obtain a white powder of  $\text{TiO}_2$ . Figure 17 shows the schematic preparation of the photocatalysts.



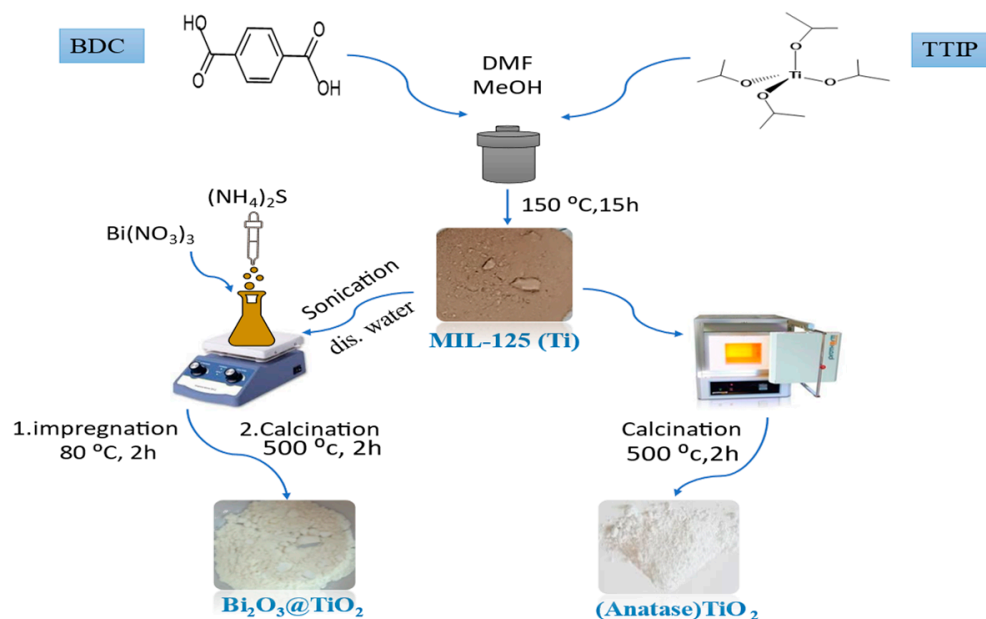


Figure 17. Schematic preparation method of photocatalysts.

### 3.3. Characterization

Nitrogen sorption isotherm analysis was carried out at  $-196\text{ }^\circ\text{C}$  on a 3H-2000PS1 Gas Sorption and Porosimeter system (Beishide Instrument Technology (BSD), Shaanxi, China). The samples were routinely prepared for evaluation after degassing at  $150\text{ }^\circ\text{C}$  under vacuum for 2 h, until the ultimate pressure reached  $1 \times 10^{-3}$  Torr. X-ray photoelectronic spectroscopy (XPS) was performed using a monochromatic X-ray Al K- $\text{AlPHA}$  (ThermoFisher Scientific, Waltham, MA, USA) with a detection threshold of 0.05%. On a Rigaku D/Max-2550 diffractometer equipped with a SolX detector CuK radiation with  $\lambda = 1.5418\text{ \AA}$  (Rigaku Corporation, Tokyo, Japan), the XRD patterns were analyzed. Using a NicoLET iS10 spectrometer, Fourier transform infrared (FT-IR) spectroscopy was performed. A Bruker Equinox 55 Fourier transform infrared spectrophotometer (Bruker Corporation, Billerica, MA, USA) was employed to capture the spectra by using the KBr pellet technique, and diffuse reflectance spectra were scanned in the range of  $500\text{--}4000\text{ cm}^{-1}$  with a resolution of  $2\text{ cm}^{-1}$  and 100 scans for each measurement. Images from scanning electron microscopy (SEM) were captured using a SUPRA 55 equipped with a 20 kV acceleration voltage (Carl Zeiss AG, Oberkochen, Germany). A transmission electron microscope (TEM, JEM-2100, JEOL Ltd., Akishima, Tokyo, Japan) and UV-visible diffuse reflectance spectrophotometer (UV-Vis DRS, Lambda 950 Perkin Elmer, Inc., Waltham, MA, USA) were employed. The  $\text{NH}_3$ -TPD analysis was performed from 25 to  $700\text{ }^\circ\text{C}$  with a heating rate of  $5\text{ }^\circ\text{C}/\text{min}$  on a catalyst analyzer BELCAT (MicrotracBEL Corp., Osaka, Japan).

### 3.4. Photocatalytic Activity

Eriochrome Black T (EBT) was dissolved in distilled water to prepare the EBT dye solution. The solution concentration was  $50\text{ mg L}^{-1}$ . A 200 W tungsten lamp was used as the visible light source. It emits a continuous spectrum that extends from visible light (around  $400\text{--}700\text{ nm}$ ) to near-infrared (NIR) wavelengths (up to about  $2500\text{ nm}$ ). A total of 50 mg of the photocatalysts was added to 50 mL of EBT solution with continuous stirring for 30 min in the dark to reach an adsorption-desorption equilibrium before irradiation. The solution was then irradiated under visible light and stirred magnetically. During the test, a specific volume of liquid (about 4 mL) was withdrawn at regular time intervals and centrifuged to eliminate the catalyst from the aqueous solution. The concentration of EBT

was determined by measuring the absorbance at 532 nm with a UV-Vis spectrophotometer. The percentage of dye degradation was calculated from Equation (3).

$$\text{Degradation}(\%) = \frac{C_i - C_f}{C_i} \times 100 \quad (3)$$

where  $C_i$  and  $C_f$  are the initial and final dye concentration, respectively. The reusability experiment is explained in the Supporting Information File.

### 3.5. Computational Methodology

The neutral EBT and protonated forms ( $\text{HEB}^{-2}(\text{O}24)$  and  $\text{EB}^{-3}$ ) were fully optimized based on the Density Functional Theory (DFT) of Becke's three-parameter and the Lee–Yang–Parr hybrid functional (B3LYP) in conjunction with the 6-311++G(d,p) basis set in liquid phase [51]. The investigated dye's electronic absorption spectra were discovered utilizing the quantum chemistry techniques TD-DFT (TD-B3LYP/6-311++G(d,p) with the spin multiplicity equal to one and the number of singlet states equal to ten [52], to analyze the UV-visible spectrum in water for comparison with experimental results. This spectrum was modelled using the Gauss-Sum program [53].

The Gaussian 09 program was used to perform all DFT and TD-DFT simulations [52]. To understand the reactivity and stability of the studied structures, global chemical reactivity descriptors [42] have been determined using the energies of the highest occupied and lowest unoccupied molecular orbitals (HOMO and LUMO). The abilities of electron-donating and electron-accepting sites have also been represented by HOMO and LUMO, respectively. Furthermore, the ionization potential (IP) and electron affinity (AE) were calculated by using the HOMO and LUMO energies through the equations  $IP = -E_{HOMO}$  and  $AE = -E_{LUMO}$ , respectively. Furthermore, the electronic chemical potential ( $\mu$ ) can be defined as Equation (4) in accordance with Koopmans' theorem [54,55].

$$\mu = -\chi = \left( \frac{\partial E}{\partial N} \right)_{v(r)} \quad (4)$$

where ( $\chi$ ) is electronegativity. The softness ( $S$ ) and hardness ( $\eta$ ) can be calculated from the first partial derivative of  $\mu$  according to  $N$  (total number of electrons), which is equal to the second derivative of the variation of energy according to the  $N$  by Equation (5):

$$\frac{1}{S} = 2\eta = \left( \frac{\partial \mu}{\partial N} \right)_{v(r)} = \left( \frac{\partial^2 E}{\partial^2 N} \right) \quad (5)$$

In addition, the  $S$ ,  $\mu$ ,  $\eta$ ,  $\omega$  (electrophilicity), and  $\Delta N_{\max}$  (charge transfer capability) values can be calculated using the frontier molecular orbital (FMO) energies as shown below [56,57].

$$S = \frac{1}{\eta} = \left( \frac{-2}{E_{HOMO} - E_{LUMO}} \right) \quad (6)$$

$$\mu = \frac{E_{HOMO} + E_{LUMO}}{2} \quad (7)$$

$$\eta = \frac{E_{LUMO} - E_{HOMO}}{2} \quad (8)$$

$$\omega = \frac{\mu^2}{2\eta} \quad (9)$$

$$\Delta N_{\max} = \frac{\chi}{2\eta} \quad (10)$$

To predict the degradation centers and reactivity of the studied neutral EBT and protonated forms ( $\text{HEB}^{-2}(\text{O}24)$  and  $\text{EB}^{-3}$ ), ESP mapping and Mulliken charges are investigated [58].

#### 4. Conclusions

In this sense, we successfully synthesized a series of  $\text{Bi}_2\text{O}_3@\text{TiO}_2$  composites for the photocatalytic degradation of both anionic and cationic organic dye pollutants using a straightforward impregnation followed by calcination, with MIL-125(Ti) as the precursor for the first time. Characterization techniques including XRD, XPS, FTIR, and SEM-EDX confirmed the successful impregnation of Bi into the  $\text{TiO}_2$  structure. Among the synthesized composites, 10%  $\text{Bi}_2\text{O}_3@\text{TiO}_2$  demonstrated superior photocatalytic performance, achieving 100% degradation efficiency of EBT dye within 30 min under visible-light irradiation, outperforming MIL-125 and  $\text{TiO}_2$ . The remarkable enhancement in photocatalytic activity can be attributed to the increased surface acidity and the formation of additional defect sites from Bi impregnation, which also facilitated the formation of hydroxyl groups via increased water molecule adsorption. Furthermore, 10%  $\text{Bi}_2\text{O}_3@\text{TiO}_2$  exhibited excellent stability, maintaining a degradation rate of 76% even after four cycles of reuse.

**Supplementary Materials:** The following supporting information can be downloaded at: <https://www.mdpi.com/article/10.3390/catal14110829/s1>, Reusability experiment, effect of different ratios of  $\text{Bi}_2\text{O}_3$ , XPS analysis, pore size distribution, photocatalytic comparison, and computational study details. **Table S1:** Acid properties of  $\text{TiO}_2$  and 10%  $\text{Bi}_2\text{O}_3@\text{TiO}_2$ ; **Figure S1:** pore size distribution of various samples; **Figure S2:** The optimized structures, FMO amplitudes (The LUMO and HOMO electron densities) for neutral EBT and protonated forms calculated by DFT/B3LYP/6-311++G(d,p) level; **Table S2:** Mulliken atomic charges of the B3LYP/6-311++G(d,p) optimized neutral and protonated EB in an aqueous medium; **Figure S3:** The contour representation of electrostatic potential regions of negative (positive) potential is red (green) for molecules; (a)  $\text{H}_2\text{EB}^-$  and (b)  $\text{HEB}^{-2}$  ( $\text{O}^{2-}$ ) in the aqueous phase using the DFT/B3LYP/6-311++G(d,p) method; **Figure S4:** The photocatalytic activity of 10%  $\text{Bi}_2\text{O}_3@\text{TiO}_2$  towards different dyes at the studied optimum conditions; **Figure S5:** The cycling runs of the degradation of EBT dye over 10%  $\text{Bi}_2\text{O}_3@\text{TiO}_2$  after regeneration; **Figure S6:** Decomposition of Lidocaine hydrochloride (0.05 g catalyst, 50 ppm 50 mL lidocaine hydrochloride solution, pH = 6, the irradiation time: 30 min) over 10%  $\text{Bi}_2\text{O}_3@\text{TiO}_2$ .

**Author Contributions:** Methodology, J.M.; Methodology and writing-original draft, A.G.A.; Methodology, writing-original draft, and Conceptualization, A.S.A.-E.; Formal analysis, Z.Z.; Funding acquisition and supervision, X.L.; Resources and Supervision, T.Z.S.; Software and supervision, S.H.E.-D. All authors have read and agreed to the published version of the manuscript.

**Funding:** The financial support from the Scientific Research Start-up Project of Shenzhen Polytechnic (6024331007K) and the Faculty of Science, Menoufia University.

**Data Availability Statement:** The data are contained within the article and Supporting Information.

**Acknowledgments:** The authors acknowledge the financial support from the Scientific Research Start-up Project of Shenzhen Polytechnic (6024331007K) and the Faculty of Science, Menoufia University. Shenzhen Polytechnic University Research Fund (6023310027K, 6024310044K) and Research Funding of Post-doctoral Who Came to Shenzhen (4103-6021271018K1).

**Conflicts of Interest:** The authors declare no conflicts of interest.

#### References

1. Rajbongshi, B.M. Photocatalyst: Mechanism, challenges, and strategy for organic contaminant degradation. In *Handbook of Smart Photocatalytic Materials*; Elsevier: Amsterdam, The Netherlands, 2020; pp. 127–149.
2. Lee, S.-Y.; Park, S.-J.  $\text{TiO}_2$  photocatalyst for water treatment applications. *J. Ind. Eng. Chem.* **2013**, *19*, 1761–1769. [[CrossRef](#)]
3. Wang, J.L.; Xu, L.J. Advanced oxidation processes for wastewater treatment: Formation of hydroxyl radical and application. *Crit. Rev. Environ. Sci. Technol.* **2012**, *42*, 251–325. [[CrossRef](#)]
4. Bedia, J.; Muelas-Ramos, V.; Peñas-Garzón, M.; Gómez-Avilés, A.; Rodríguez, J.J.; Bolver, C. A review on the synthesis and characterization of metal organic frameworks for photocatalytic water purification. *Catalysts* **2019**, *9*, 52. [[CrossRef](#)]
5. Wang, J.-C.; Cui, C.-X.; Li, Y.; Liu, L.; Zhang, Y.-P.; Shi, W. Porous Mn doped g-C<sub>3</sub>N<sub>4</sub> photocatalysts for enhanced synergetic degradation under visible-light illumination. *J. Hazard. Mater.* **2017**, *339*, 43–53. [[CrossRef](#)]
6. Wang, M.; Yang, L.; Yuan, J.; He, L.; Song, Y.; Zhang, H.; Zhang, Z.; Fang, S. Heterostructured  $\text{Bi}_2\text{S}_3@\text{NH}_2\text{-MIL-125(Ti)}$  nanocomposite as a bifunctional photocatalyst for Cr(VI) reduction and rhodamine B degradation under visible light. *RSC Adv.* **2018**, *8*, 12459–12470. [[CrossRef](#)]

7. Li, D.; Shi, W. Recent developments in visible-light photocatalytic degradation of antibiotics. *Chin. J. Catal.* **2016**, *37*, 792–799. [[CrossRef](#)]
8. Haghghat, G.A.; Sadeghi, S.; Saghi, M.H.; Ghadiri, S.K.; Anastopoulos, I.; Giannakoudakis, D.A.; Colmenares, J.C.; Shams, M. Zeolitic imidazolate frameworks (ZIFs) of various morphologies against eriochrome black-T (EBT): Optimizing the key physicochemical features by process modeling. *Colloids Surf. A Physicochem. Eng. Asp.* **2020**, *606*, 125391. [[CrossRef](#)]
9. Honarmand, M.; Golmohammadi, M.; Hafezi-Bakhtiari, J. Synthesis and characterization of SnO<sub>2</sub> NPs for photodegradation of eriochrome black-T using response surface methodology. *Environ. Sci. Pollut. Res.* **2021**, *28*, 7123–7133. [[CrossRef](#)]
10. Honarmand, M.; Golmohammadi, M.; Naeimi, A. Green synthesis of SnO<sub>2</sub>-bentonite nanocomposites for the efficient photodegradation of methylene blue and eriochrome black-T. *Mater. Chem. Phys.* **2020**, *241*, 122416. [[CrossRef](#)]
11. Kansal, S.K.; Sood, S.; Umar, A.; Mehta, S.K. Photocatalytic degradation of Eriochrome Black T dye using well-crystalline anatase TiO<sub>2</sub> nanoparticles. *J. Alloys Compd.* **2013**, *581*, 392–397. [[CrossRef](#)]
12. Khnifira, M.; Boumya, W.; Abdennouri, M.; Sadiq, M.H.; Achak, M.; Serdaroğlu, G.; Kaya, S.; Şimşek, S.; Barka, N. A combined molecular dynamic simulation, DFT calculations, and experimental study of the eriochrome black T dye adsorption onto chitosan in aqueous solutions. *Int. J. Biol. Macromol.* **2021**, *166*, 707–721. [[CrossRef](#)] [[PubMed](#)]
13. Singh, S.; Kumari, P.; Tripathi, S.; Singh, G.; Kaura, A. The mechanism of tuning the morphology of bio-conjugated ZnO nanoparticles with citrate coated gold nanoparticles for degradation of EBT: DFT and experimental study. *J. Mol. Liq.* **2019**, *295*, 111706. [[CrossRef](#)]
14. Zhang, C.; Wei, S.; Sun, L.; Xu, F.; Huang, P.; Peng, H. Synthesis, structure and photocatalysis properties of two 3D Isostructural Ln (III)-MOFs based 2, 6-Pyridinedicarboxylic acid. *J. Mater. Sci. Technol.* **2018**, *34*, 1526–1531. [[CrossRef](#)]
15. Yue, K.; Zhang, X.; Jiang, S.; Chen, J.; Yang, Y.; Bi, F.; Wang, Y. Recent advances in strategies to modify MIL-125(Ti) and its environmental applications. *J. Mol. Liq.* **2021**, *335*, 116108. [[CrossRef](#)]
16. Wang, Q.; Wang, G.; Liang, X.; Dong, X.; Zhang, X. Supporting carbon quantum dots on NH<sub>2</sub>-MIL-125 for enhanced photocatalytic degradation of organic pollutants under a broad spectrum irradiation. *Appl. Surf. Sci.* **2019**, *467–468*, 320–327. [[CrossRef](#)]
17. Grau-Crespo, R.; Aziz, A.; Collins, A.W.; Crespo-Otero, R.; Hernández, N.C.; Rodríguez-Albelo, L.M.; Ruiz-Salvador, A.R.; Calero, S.; Hamad, S. Modelling a linker mix-and-match approach for controlling the optical excitation gaps and band alignment of zeolitic imidazolate frameworks. *Angew. Chem.* **2016**, *128*, 16246–16250. [[CrossRef](#)]
18. Meyer, K.; Bashir, S.; Llorca, J.; Idriss, H.; Ranocchiari, M.; van Bokhoven, J.A. Photocatalyzed hydrogen evolution from water by a composite catalyst of NH<sub>2</sub>-MIL-125(Ti) and surface nickel (II) species. *Chem. A Eur. J.* **2016**, *22*, 13894–13899. [[CrossRef](#)]
19. Zhu, S.-R.; Liu, P.-F.; Wu, M.-K.; Zhao, W.-N.; Li, G.-C.; Tao, K.; Yi, F.-Y.; Han, L. Enhanced photocatalytic performance of BiOBr/NH<sub>2</sub>-MIL-125(Ti) composite for dye degradation under visible light. *Dalton Trans.* **2016**, *45*, 17521–17529. [[CrossRef](#)]
20. Wu, D.; Han, L. Fabrication of novel Ag/AgBr/NH<sub>2</sub>-MIL-125(Ti) nanocomposites with enhanced visible-light photocatalytic activity. *Mater. Res. Express* **2019**, *6*, 125501. [[CrossRef](#)]
21. Yin, S.; Chen, Y.; Gao, C.; Hu, Q.; Li, M.; Ding, Y.; Di, J.; Xia, J.; Li, H. In-situ preparation of MIL-125(Ti)/Bi<sub>2</sub>WO<sub>6</sub> photocatalyst with accelerating charge carriers for the photodegradation of tetracycline hydrochloride. *J. Photochem. Photobiol. A Chem.* **2020**, *387*, 112149. [[CrossRef](#)]
22. Jia, J.; Wang, Y.; Xu, M.; Qi, M.-l.; Wu, Y.; Zhao, G. MOF-derived the direct Z-scheme g-C<sub>3</sub>N<sub>4</sub>/TiO<sub>2</sub> with enhanced visible photocatalytic activity. *J. Sol-Gel Sci. Technol.* **2020**, *93*, 123–130. [[CrossRef](#)]
23. Guo, H.; Lin, F.; Chen, J.; Li, F.; Weng, W. Metal-organic framework MIL-125(Ti) for efficient adsorptive removal of Rhodamine B from aqueous solution. *Appl. Organomet. Chem.* **2015**, *29*, 12–19. [[CrossRef](#)]
24. Bhadra, B.N.; Song, J.Y.; Khan, N.A.; Jhung, S.H. TiO<sub>2</sub>-containing carbon derived from a metal-organic framework composite: A highly active catalyst for oxidative desulfurization. *ACS Appl. Mater. Interfaces* **2017**, *9*, 31192–31202. [[CrossRef](#)] [[PubMed](#)]
25. Zatsopin, D.; Boukhvalov, D.; Gavrillov, N.; Kurmaev, E.; Zhidkov, I. XPS and DFT study of pulsed Bi-implantation of bulk and thin-films of ZnO—The role of oxygen imperfections. *Appl. Surf. Sci.* **2016**, *387*, 1093–1099. [[CrossRef](#)]
26. George, P.; Dhabarde, N.R.; Chowdhury, P. Rapid synthesis of titanium based metal organic framework (MIL-125) via microwave route and its performance evaluation in photocatalysis. *Mater. Lett.* **2017**, *186*, 151–154. [[CrossRef](#)]
27. Ali, S.S. The Influence of Synthesized TiO<sub>2</sub>-Nanoparticles on the Performance of Inks Utilized in Printing Documents. *J. Chem. Soc. Pak.* **2023**, *45*, 382.
28. Prabhu, S.; Nithya, A.; Mohan, S.C.; Jothivenkatachalam, K. Synthesis, surface acidity and photocatalytic activity of WO<sub>3</sub>/TiO<sub>2</sub> nanocomposites—An overview. *Mater. Sci. Forum* **2014**, *781*, 63–78. [[CrossRef](#)]
29. Chen, J.; Zhang, X.; Bi, F.; Zhang, X.; Yang, Y.; Wang, Y. A facile synthesis for uniform tablet-like TiO<sub>2</sub>/C derived from Materials of Institut Lavoisier-125(Ti)(MIL-125(Ti)) and their enhanced visible light-driven photodegradation of tetracycline. *J. Colloid Interface Sci.* **2020**, *571*, 275–284. [[CrossRef](#)]
30. Zhou, Y.; Li, Q.; Zhang, J.; Xiang, M.; Zhou, Y.; Chen, Z.; Chen, Y.; Yao, T. Broad spectrum driven Y doped BiO<sub>2-x</sub> for enhanced degradation of tetracycline: Synergy between singlet oxygen and free radicals. *Appl. Surf. Sci.* **2023**, *607*, 154957. [[CrossRef](#)]
31. Aisien, F.; Amenaghawon, N.; Ekpenisi, E. Photocatalytic decolourisation of industrial wastewater from a soft drink compan. *J. Eng. Appl. Sci.* **2013**, *9*, 11–16.
32. Jamal, N.; Radhakrishnan, A.; Raghavan, R.; Bhaskaran, B. Efficient photocatalytic degradation of organic dye from aqueous solutions over zinc oxide incorporated nanocellulose under visible light irradiation. *Main Group Met. Chem.* **2020**, *43*, 84–91. [[CrossRef](#)]

33. Hemmatpour, P.; Nezamzadeh-Ejehieh, A.; Ershadi, A. A brief study on the Eriochrome Black T photodegradation kinetic by CdS/BiVO<sub>4</sub> coupled catalyst. *Mater. Res. Bull.* **2022**, *151*, 111830. [CrossRef]
34. Najjar, M.; Hosseini, H.A.; Masoudi, A.; Sabouri, Z.; Mostafapour, A.; Khatami, M.; Darroudi, M. Green chemical approach for the synthesis of SnO<sub>2</sub> nanoparticles and its application in photocatalytic degradation of Eriochrome Black T dye. *Optik* **2021**, *242*, 167152. [CrossRef]
35. Hunge, Y.M.; Yadav, A.A.; Kang, S.-W. Photocatalytic degradation of eriochrome black-T using BaWO<sub>4</sub>/MoS<sub>2</sub> Composite. *Catalysts* **2022**, *12*, 1290. [CrossRef]
36. Hassan, F.; Bonnet, P.; Dangwang Dikdim, J.M.; Gatcha Bandjoun, N.; Caperaa, C.; Dalhatou, S.; Kane, A.; Zeghioud, H. Synthesis and investigation of TiO<sub>2</sub>/g-C<sub>3</sub>N<sub>4</sub> performance for photocatalytic degradation of bromophenol blue and Eriochrome Black T: Experimental design optimization and reactive oxygen species contribution. *Water* **2022**, *14*, 3331. [CrossRef]
37. De, I.; Pahuja, M.; ud din Wani, H.M.; Dey, A.; Dube, T.; Ghosh, R.; Kankan, N.; Mishra, J.; Panda, J.J.; Maruyama, T. In-vitro toxicity assessment of a textile dye Eriochrome Black T and its nano-photocatalytic degradation through an innovative approach using Mf-NGr-CNTs-SnO<sub>2</sub> heterostructures. *Ecotoxicol. Environ. Saf.* **2022**, *243*, 113985. [CrossRef]
38. Golmohammadi, M.; Hassankiadeh, M.N.; Zhang, L. Facile biosynthesis of SnO<sub>2</sub>/ZnO nanocomposite using *Acroptilon repens* flower extract and evaluation of their photocatalytic activity. *Ceram. Int.* **2021**, *47*, 29303–29308. [CrossRef]
39. El-Katori, E.E.; Kasim, E.A.; Ali, D.A. Sol-gel synthesis of mesoporous NiO/ZnO heterostructure nanocomposite for photocatalytic and anticorrosive applications in aqueous media. *Colloids Surf. A Physicochem. Eng. Asp.* **2022**, *636*, 128153. [CrossRef]
40. Liu, S.-j.; Li, F.-t.; Li, Y.-l.; Hao, Y.-j.; Wang, X.-j.; Li, B.; Liu, R.-h. Fabrication of ternary g-C<sub>3</sub>N<sub>4</sub>/Al<sub>2</sub>O<sub>3</sub>/ZnO heterojunctions based on cascade electron transfer toward molecular oxygen activation. *Appl. Catal. B Environ.* **2017**, *212*, 115–128. [CrossRef]
41. Chafai, N.; Chafaa, S.; Benbouguerra, K.; Daoud, D.; Hellal, A.; Mehri, M. Synthesis, characterization and the inhibition activity of a new  $\alpha$ -aminophosphonic derivative on the corrosion of XC48 carbon steel in 0.5 M H<sub>2</sub>SO<sub>4</sub>: Experimental and theoretical studies. *J. Taiwan Inst. Chem. Eng.* **2017**, *70*, 331–344. [CrossRef]
42. Miar, M.; Shiroudi, A.; Pourshamsian, K.; Oliaey, A.R.; Hatamjafari, F. Theoretical investigations on the HOMO–LUMO gap and global reactivity descriptor studies, natural bond orbital, and nucleus-independent chemical shifts analyses of 3-phenylbenzo[d]thiazole-2(3H)-imine and its para-substituted derivatives: Solvent and substituent effects. *J. Chem. Res.* **2021**, *45*, 147–158.
43. Omer, R.; Koparır, P.; Ahmed, L.; Koparır, M. Computational determination the reactivity of salbutamol and propranolol drugs. *Turk. Comput. Theor. Chem.* **2020**, *4*, 67–75. [CrossRef]
44. Sıdır, İ.; Sıdır, Y.G.; Kumalar, M.; Taşal, E. Ab initio Hartree–Fock and density functional theory investigations on the conformational stability, molecular structure and vibrational spectra of 7-acetoxy-6-(2,3-dibromopropyl)-4, 8-dimethylcoumarin molecule. *J. Mol. Struct.* **2010**, *964*, 134–151. [CrossRef]
45. Jug, K.; Maksić, Z.B. The Meaning and Distribution of Atomic Charges in Molecules. In *Theoretical Models of Chemical Bonding: Molecular Spectroscopy, Electronic Structure and Intramolecular Interactions Part 3*; Springer: Berlin/Heidelberg, Germany, 1991; pp. 235–288.
46. Hasnat, M.; Siddiquey, I.; Nuruddin, A. Comparative photocatalytic studies of degradation of a cationic and an anionic dye. *Dye. Pigment.* **2005**, *66*, 185–188. [CrossRef]
47. Rayaroth, M.P.; Aravind, U.K.; Aravindakumar, C.T. Photocatalytic degradation of lignocaine in aqueous suspension of TiO<sub>2</sub> nanoparticles: Mechanism of degradation and mineralization. *J. Environ. Chem. Eng.* **2018**, *6*, 3556–3564. [CrossRef]
48. Tao, L.; Zhang, H.; Li, G.; Liao, C.; Jiang, G. Photocatalytic degradation of pharmaceuticals by pore-structured graphitic carbon nitride with carbon vacancy in water: Identification of intermediate degradants and effects of active species. *Sci. Total Environ.* **2022**, *824*, 153845. [CrossRef]
49. Nichols, L. Stability of Lidocaine Tested by Forced Degradation and its Interactions with Serum Albumin. 2015. Available online: <https://digitalcommons.calpoly.edu/star/341/> (accessed on 7 October 2024).
50. Abou-Elyazed, A.S.; Li, S.; Mohamed, G.G.; Li, X.; Meng, J.; EL-Sanafery, S.S. Graphitic Carbon Nitride/MOFs Hybrid Composite as Highly Selective and Sensitive Electrodes for Calcium Ion Detection. *Molecules* **2023**, *28*, 8149. [CrossRef]
51. Frisch, M. *Gaussian 09, Revision D. 01*; Gaussian Inc.: Wallingford, CT, USA, 2009; Volume 201.
52. Halim, S.A.; Ibrahim, M.A. Quantum computational, Spectroscopic investigations on benzofuranlycarbonylpyrazolopyridine by DFT/TD-DFT: Synthesis, Structure, NBO and NLO research. *J. Mol. Struct.* **2023**, *1293*, 136201. [CrossRef]
53. El-Meligy, A.B.; Koga, N.; Iuchi, S.; Yoshida, K.; Hirao, K.; Mangood, A.H.; El-Nahas, A.M. DFT/TD-DFT calculations of the electronic and optical properties of bis-N,N-dimethylaniline-based dyes for use in dye-sensitized solar cells. *J. Photochem. Photobiol. A Chem.* **2018**, *367*, 332–346. [CrossRef]
54. Obot, I.; Gasem, Z. Theoretical evaluation of corrosion inhibition performance of some pyrazine derivatives. *Corros. Sci.* **2014**, *83*, 359–366. [CrossRef]
55. Abou-Elyazed, A.; Sun, Y.; El-Nahas, A.; Abdel-Azeim, S.; Sharara, T.; Yousif, A. Solvent-free synthesis and characterization of Ca<sup>2+</sup>-doped UiO-66(Zr) as heterogeneous catalyst for esterification of oleic acid with methanol: A joint experimental and computational study. *Mater. Today Sustain.* **2022**, *18*, 100110. [CrossRef]
56. Obot, I.; Macdonald, D.; Gasem, Z. Density functional theory (DFT) as a powerful tool for designing new organic corrosion inhibitors. Part 1: An overview. *Corros. Sci.* **2015**, *99*, 1–30. [CrossRef]

57. Liu, P.; Fang, X.; Tang, Y.; Sun, C.; Yao, C. Electrochemical and quantum chemical studies of 5-substituted tetrazoles as corrosion inhibitors for copper in aerated 0.5 M H<sub>2</sub>SO<sub>4</sub> solution. *Mater. Sci. Appl.* **2011**, *2*, 1268–1278.
58. Mulliken, R.S. Electronic population analysis on LCAO–MO molecular wave functions. I. *J. Chem. Phys.* **1955**, *23*, 1833–1840. [[CrossRef](#)]

**Disclaimer/Publisher’s Note:** The statements, opinions and data contained in all publications are solely those of the individual author(s) and contributor(s) and not of MDPI and/or the editor(s). MDPI and/or the editor(s) disclaim responsibility for any injury to people or property resulting from any ideas, methods, instructions or products referred to in the content.